Rotational Excitation of Interstellar OCS: Non-LTE Line Analysis and Temperature–Density Diagnostics Using RADEX

A thesis submitted for the degree of

Bachelor of Science
in
Astronomy

by

ZALÁN NOVÁK
5053757

Supervisor: dr. F.F.S. (Floris) van der Tak

Faculty of Science and Engineering
University of Groningen
Groningen, the Netherlands

Abstract

In this study, the potential of the OCS molecule was investigated as a tracer of temperature and density in different astrophysical environments through modeling of its rotational line emission using the non-LTE radiative transfer code `RADEX`. The work included analysis of modeled line intensities, diagnostics based on previous observations, and the development of a future observing proposal targeting the L1157 nebula. For the observations, the IRAM 30m telescope is proposed with an estimated total telescope time of 16 hours, and it aims to further test OCS as an environmental condition tracer in shocked molecular regions. The results suggest that rotational transitions of OCS can be used to constrain the kinetic temperature and density in molecular clouds, star-forming regions, and the Galactic Center, and may also serve as a temperature probe in protoplanetary disks. At temperatures and densities higher than ~ 100 K and $\sim 10^6$ cm^{-3}, the applicability of OCS is limited due to the lack of collisional rate coefficients and line transitions exceeding critical densities. Nevertheless, OCS remains a promising candidate for constraining environmental properties and could provide further insight into the conditions of the interstellar medium due to its unique property of having significantly closer rotational energy levels than other interstellar molecules. To draw more rigorous conclusions about OCS line diagnostics, additional observations across a broader range of environments are encouraged. Future studies would also benefit from using advanced radiative transfer codes like `ProDiMo` or `LIME`, which can account for three-dimensional structures, as well as temperature and density gradients in the complex molecular regions where OCS emission is modeled.

Contents

Chapter 1

Introduction

The study of the interstellar medium (ISM) remains one of the most significant yet incompletely understood areas of astrophysics. Understanding the ISM requires complex approaches, as it contains various phases of matter, including atomic, molecular, and ionized gases, as well as dust, which participate in different physical and chemical processes. The gas cycle within galaxies is one such process that sets the environmental conditions for interstellar chemistry, star formation, and the formation of planetary systems. Stars form in dark molecular clouds (MCs), evolve through protostellar phases, and eventually give rise to planetary systems before ending their life cycles. One of the main reasons for studying star formation is to understand how this gas cycle works and how planetary systems develop and evolve. The characteristics of the ISM that lead to the formation of these astrophysical objects, including background radiation, temperature, and density, are important as they directly influence the properties of the observed evolutionary stages. In this section, the importance of interstellar molecules in the study of the ISM and different astrophysical regions is outlined, with a focus on OCS as a new candidate for temperature and density diagnostics.

1.1. Molecules in the ISM

A common feature across stellar and planetary evolutionary stages is the presence of molecules. Molecules have been identified in the interstellar medium since 1937, when the first interstellar molecule, CH, was observed in the optical spectrum at 430 nm [1]. To date, more than 300 molecules have been detected in the ISM [2]. These interstellar molecules serve as essential tools for probing the physical conditions and dynamics within these regions through their emission and absorption lines at millimeter and submillimeter wavelengths.

As molecules can be dissociated via collisions and strong UV radiation (especially in photon-dominated regions (PDRs)), their presence requires a relatively cold interstellar medium. Due to the cold ($\sim 10 -$ few 100 K) nature of these molecular environments, rotational transitions dominate their spectra. This is because vibrational and electronic transitions require much higher energies and consequently higher temperatures: electronic transitions happen at energies in the eV range corresponding to UV/visible light, compared to vibrational transitions, which require about $0.01 - 0.1$ eV in the infrared range, and rotational transitions, which need only about $0.001 - 0.01$ eV in the radio to far infrared wavelengths [3]. The energy levels involved in rotational transitions are relatively closely spaced, making them sensitive to the low temperatures typical of molecular regions. Some of the most important submillimeter observations of molecular regions have been made by the Caltech Submillimeter Observatory (CSO), the Atacama Large Millimeter

Array (ALMA), the Northern Extended Millimeter Array (NOEMA), and the 30m telescope of the Institut de Radioastronomie Millimetrique (IRAM) [1].

Understanding the mechanisms behind rotational excitation and molecular line emission is crucial to tracing physical properties such as temperature and density. Rotational transitions can be induced by radiation or collisions with other molecules. As these molecular regions are often not in local thermodynamic equilibrium (LTE) due to significant density variations, radiative excitation becomes very important, especially in low-density regions. Under non-LTE conditions, the intensity and profile of molecular lines can provide valuable information about the physical conditions present.

The most important collision partner in the ISM and other molecular regions that can lead to molecular excitation is molecular hydrogen (H_2), as it is by far the most abundant molecule. Since H_2 has no permanent dipole moment and its rotational excitation requires high temperatures of hundreds of Kelvins, it is not useful for probing molecular regions because it does not emit detectable electromagnetic radiation [4]. The most abundant molecular species that can be observed are constructed from the most common chemically reactive elements: H, O, C, N, and S, which allow for a myriad of molecular combinations. Among them, sulfur-bearing molecules are of special interest as a result of their observed underabundances in the gas phase.

1.2. Interstellar OCS

One such molecule is carbonyl sulfide (OCS), which has been detected in a wide variety of astrophysical environments, including star-forming regions (SFRs), protoplanetary disks (PPDs), and extragalactic starburst galaxies [5][6][7]. Its first observation in the ISM was made in 1977 by Hollis et al. [8] using the Green Bank Telescope (GBT), with the detection occurring in a molecular cloud in the Taurus-Auriga complex. This was a pivotal discovery, as it marked OCS as one of the first sulfur-bearing molecules detected in the ISM, providing insight into the sulfur chemistry and molecular composition of interstellar clouds.

The interstellar sulfur cycle is not a fully understood process, as the amount of sulfur expected and observed in different astrophysical regions does not match [9]. This discrepancy hints that there is a gap between our understanding of how sulfur is cycled through different phases and chemical forms in the ISM. OCS is one of the candidates that could explain this discrepancy, as a large fraction of it is frozen out as ice, which is harder to observe than free molecules.

Since its first detection, OCS has been observed in the atmospheres of planets such as Venus and Jupiter [10][11], and it is one of the only two sulfur-containing molecules (together with SO_2) detected in solid ices [12]. OCS helped trace the origin of cometary ices and contributed to our understanding of the molecular composition of protoplanetary disks [6][13], and it also plays a significant role in astrobiology due to its correlation with methanol (CH_3OH), a simple organic molecule that serves as a precursor to more complex organics [14].

Observations confirm that OCS can form through various chemical pathways in the ISM, including reactions on the surfaces of dust grains and in the gas phase. Analyzing the abundances and distributions of different molecules allows astronomers to infer the chemical networks and pathways that govern interstellar chemistry. It has been demonstrated by Hawkins et al. [15] that CO molecules can capture S atoms, resulting in one of the most common pathways for the formation of OCS. This is generally considered to be the reaction involving the dissociation of excited H_2S into H and HS radicals, which is then further dissociated to obtain an S atom that is captured by the CO molecule [16]:

$$H_2S \rightarrow 2H + S$$

$$S + CO \rightarrow OCS.$$

With sulfur contributing to more than 20 known interstellar molecules and CO being the second most abundant molecule after H_2 [17], OCS is a key tracer of interstellar sulfur chemistry in the cold molecular gas.

Gas-phase OCS is mainly dissociated via collisions with CH, resulting in the production of CO and HCS [18]. The approximate rate at which this reaction occurs at 150 K is 4×10^{-10} cm^3 s^{-1} as calculated by Lucas et al. [18], which implies that this form of OCS dissociation in cold environments is significantly more frequent than the average molecular dissociation rate of $\lesssim 10^{-15}$ s^{-1} expected from cosmic rays [19].

1.3. Environmental Diagnostics and the Potential of OCS

Although OCS is among the 20 most abundant interstellar molecules and has been identified in many astrophysical regions [20], it has not been widely used to constrain the physical conditions of these regions. In contrast to OCS, several other molecules are commonly used to investigate physical parameters, which are listed in Table 1 together with the ranges of parameters they probe and the environments in which they are most commonly used.

Table 1: Summary of the most abundant interstellar molecules that are used for probing environmental conditions in different astrophysical regions.

Molecule	Abund. (X/H_2)	T_{kin} [K]	n(H_2) [cm^{-3}]	Useful In	Ref.
CS	$\sim 10^{-9}$	10–100	10^4–10^6	Dense cores, PPDs, MCs	[21]
N_2H^+	$\sim 10^{-10}$	10–30	10^4–10^6	Starless cores	[22]
HCN	$\sim 10^{-8}$	20–100	10^5–10^7	PDRs, dense clumps, PPDs	[23]
HCO^+	$\sim 10^{-9}$	20–100	10^4–10^6	Protostellar envelopes, PDRs	[24]
CH_3CN	$\sim 10^{-10}$	50–300	10^5–10^7	Hot cores SFRs, disks	[25]
CH_3OH	$\sim 10^{-8}$	10–200	10^4–10^7	Outflows, shocks	[26]
H_2CO	$\sim 10^{-9}$	20–100	10^4–10^6	Dense cores, SFRs	[27]

OCS exhibits a fractional abundance comparable to the molecules listed in Table 1, suggesting its potential as a diagnostic tracer in various astrophysical environments [20]. Its dissociation energies–3.73 eV for the C–S bond and 7.75 eV for the C–O bond [28]–are similar to those of other interstellar molecules, indicating a reasonable level of stability against collisions and strong background radiation [29][30].

It also shares a similar linear structure and chemical behavior with CO_2, a molecule of central interest in astrochemistry due to its role in the carbon and oxygen cycles and its presence in icy grain mantles [31]. Although CO_2 is significant for the study of chemical evolution and planet-forming material, its lack of a permanent dipole moment makes it undetectable in the radio regime, limiting our ability to study it in the gas phase. OCS, on the other hand, has a permanent dipole moment and is readily detectable through its rotational transitions. Despite lacking hydrogen–a common feature of many interstellar molecules–OCS is surprisingly abundant in a wide range of astrophysical environments. These characteristics make OCS a valuable chemical and physical proxy for CO_2 in interstellar studies.

OCS is a special molecule because its rotational energy levels are relatively close to each other compared to those of other molecules due to its large mass. Most molecules used to trace environmental conditions typically consist only of two atoms heavier than hydrogen (see Table 1), making OCS a new type of candidate for astrophysical diagnostics. For OCS, higher rotational levels are generally relatively easy to excite, which means that the neighboring line transitions usually have similar intensities, making the molecular line emission especially sensitive to temperature and density changes. This sensitivity could lead to robust estimates for temperatures and densities, as significantly different measured intensities also indicate significantly different measured line intensities.

1.4. New Collisional Data

Analyzing rotational transitions of OCS for temperature and density tracing requires knowledge of the collisional excitation rate coefficients. As H_2 is the most common collision partner in the ISM, this is most important for the H_2-OCS collisional system. The first set of collisional excitation rate coefficients for OCS with H_2 between 10 K and 100 K and up to $J = 12$ was calculated by Green et al. [32], which has been used for collisional modeling with OCS since 1978. To reduce the large amount of computation required to determine these collision coefficients *ab initio* (that is, by solving quantum mechanical equations directly for the system), their calculations were significantly simplified by using different scattering and classical mechanical approximations [32]. Extrapolation to higher levels up to $J = 99$ for temperatures between 100 K and 500 K was carried out by Schöier et al. [33].

Explicitly calculating the rate coefficients for the H_2-OCS system is quite complex, since H_2 is not a spherical collision partner. A common approach to overcome this complexity is to first compute the rate coefficients assuming that helium is the partner instead of H_2, which significantly simplifies the problem. H_2 and He differ in their collision physics, although their van der Waals (VDW) radii are similar [34][35]. The most important distinction between H_2 and He as collision partners is their mass difference, which affects their collisional rate coefficients with OCS by changing the thermal velocity distribution. Nevertheless, the similarity of their VDW radii suggests that the energy dependence of their cross sections may be similar, as both particles are neutral. Therefore, the 1978 He-OCS rate coefficients calculated from the interaction potential of the system were rescaled by the corresponding reduced mass of the H_2-OCS system in the study in Green et al. [32]. This approximation was further supported by the fact that the ground state of the hydrogen molecule with $J = 0$ behaves similarly to spherically symmetric collisional partners.

For the He-OCS collisional system, new collisional rate coefficients were provided by Denis-Alpizar et al. [36] in 2023 via ab initio calculations between 10 K and 80 K and up to $J = 40$, forming an ideal basis for new studies with OCS. The rescaling method remains a good approximation for the H_2–OCS system, with improved accuracy due to the use of quantum mechanical calculations over classical approaches.

This research explores OCS as a potential new molecule for diagnostics in different astrophysical regions using the new collisional data for the He-OCS system through this rescaling approach. For the analysis, `RADEX`, a non-LTE radiative transfer code is used to solve the statistical equilibrium and radiative transfer equations to model OCS line emission in different astrophysical environments. The original formulation of the code was developed by J. H. Black, with subsequent modifications for easier usability and direct astrophysical applications implemented by F. F. S. van der Tak (see the work of Van der Tak et al. [37] for details about the code).

Chapter 2

Theory

Molecular rotational line emission is a complex process that depends on quantum mechanical interactions, local thermodynamic conditions, and the background radiation field experienced by the molecule. The combination of these effects leads to unique line spectra in different astrophysical regions, which can be used to study the interstellar medium.

2.1. Rotational Energy Levels

OCS can be regarded as a linear rigid rotor, meaning that it is assumed to maintain its shape during rotation. Since a linear rotor is symmetric about its internuclear axis, its energy levels can be written as

$$E_J = BJ(J+1), \tag{2.1}$$

where J is the total angular momentum quantum number, and B is the rotational constant [3]. The spacing between adjacent rotational energy levels is then given by

$$F_J = E_{J+1} - E_J = 2B(J+1), \tag{2.2}$$

indicating that the energy level spacing increases linearly with J. Consequently, the energy difference between rotational line transitions is

$$\Delta F = F_{J+1} - F_J = 2B, \tag{2.3}$$

resulting in a rotational spectrum that consists of evenly spaced lines separated by $2B$.

Given that the rotational constant of OCS is $B = 2.029$ cm^{-1} [38], we can estimate the most useful frequency range of its rotational transitions for this study. For example, the lowest transition $J = 1 \rightarrow 0$ occurs at approximately 12.16 GHz, and a high-J transition like $J = 40 \rightarrow 39$ occurs at around 474.04 GHz. Transitions at such high rotational levels are rarely observed due to the low population of the corresponding energy states. For example, the $J = 40 \rightarrow 39$ transition requires an excitation energy equivalent to a kinetic temperature of nearly 500 K. Furthermore, the new collisional de-excitation coefficients have only been determined via ab into calculations up to $J = 40$, making the 10–500 GHz spectral window especially important for this study.

2.2. Radiative Transfer

The theory of radiative transfer provides the fundamental framework for understanding how electromagnetic radiation propagates through astrophysical environments, where interactions with matter occur through absorption, emission, and scattering processes. For interstellar molecules, these radiative processes govern the population dynamics of molecular energy levels, making radiative transfer essential for interpreting molecular line observations. The framework described in this section for this theory was adopted from Wilson et al. [39].

2.2.1 Solving the Radiative Transfer Equation

The radiation field within a medium can be characterized by the specific intensity I_ν, defined as the energy dE flowing through an area element $d\sigma$ per unit time dt, per unit solid angle $d\Omega$, and per unit frequency interval $d\nu$:

$$I_\nu = \frac{dE}{dt\, d\sigma\, \cos\theta\, d\Omega\, d\nu}, \tag{2.4}$$

where θ denotes the angle between the radiation propagation direction and the normal to the surface element $d\sigma$. The competition between absorption and emission processes yields the fundamental equation of radiative transfer:

$$\frac{dI_\nu}{ds} = -\kappa_\nu I_\nu + \epsilon_\nu, \tag{2.5}$$

where κ_ν represents the frequency-dependent absorption coefficient, and ϵ_ν represents the energy emitted per unit volume per unit time per unit solid angle per unit frequency. Under conditions of thermodynamic equilibrium, the intensity remains constant and equals the source function $S_\nu(T) \equiv \epsilon_\nu/\kappa_\nu$. The emission and absorption coefficients can be expressed in terms of the Einstein coefficients:

$$\epsilon_\nu = \frac{h\nu}{4\pi} n_u A_{ul} \phi(\nu) \tag{2.6}$$

$$\kappa_\nu = \frac{h\nu}{4\pi} (n_l B_{lu} - n_u B_{ul}) \phi(\nu), \tag{2.7}$$

where n_l and n_u represent the population densities of the lower and upper energy states, respectively, A_{ul} is the Einstein spontaneous emission coefficient, B_{lu} and B_{ul} are the absorption and stimulated emission coefficients, and $\phi(\nu)$ denotes the normalized line profile function that describes the frequency distribution of the spectral line. Using Eqs. 2.6 and 2.7, the source function can therefore be expressed as

$$S_\nu = \frac{A_{ul} n_u}{B_{lu} n_l - B_{ul} n_u}. \tag{2.8}$$

It is convenient to reformulate the transfer equation using the optical depth τ_ν, defined through the differential relation $d\tau_\nu \equiv -\kappa_\nu ds$. This transformation allows us to solve Eq 2.5 for a medium with total optical depth τ_0 along the line of sight with the general solution of

$$I_\nu(\tau_0) = I_\nu(0) e^{-\tau_0} + \int_0^{\tau_0} S_\nu(\tau_\nu) e^{-(\tau_0 - \tau_\nu)} d\tau_\nu, \tag{2.9}$$

where $I_\nu(0)$ represents the intensity of the background radiation incident on the medium.

To find the total intensity seen by the observer at the line frequency ν, one can explicitly solve Eq. 2.9 by assuming the source function to be equal to the Planck function B_ν at the so-called excitation temperature of the line. The excitation temperature $T_{\rm ex}$ is defined as the temperature at which a Boltzmann distribution would produce the same relative level populations. It is important to note that in a multilevel system, each transition can have its own unique excitation temperature. By this definition, we can write $S_\nu = B_\nu(T_{\rm ex})$, so that the measured line intensity can be written as

$$\Delta I_\nu = I_\nu^{\rm tot,obs} - I_\nu^{\rm bg,obs} = \left(B_\nu(T_{\rm ex}) - I_\nu^{\rm bg,obs}\right)\left(1 - e^{-\tau_0}\right). \tag{2.10}$$

In case of a region where dust emission is non-negligible, both the CMB and dust (with temperature T_d) emission contribute to the background intensity as

$$I_\nu^{\rm bg,obs} = B_\nu(T_{\rm CMB}) + B_\nu(T_d)(1 - e^{-\tau_0}). \tag{2.11}$$

2.2.2 The Radiometer Equation

To be able to directly compare these intensities with measured antenna temperatures, the Rayleigh-Jeans equivalent radiation temperature is typically used [39], given by

$$T_R \equiv \frac{c^2}{2k\nu^2}\Delta I_\nu. \tag{2.12}$$

With this definition, the radiometer equation can be used as an easy tool to evaluate whether a molecular line transition can be detected within certain observational limits. The equation describes the RMS error in the measured antenna temperature σ_{T_A} based on the observed frequency bandwidth $\Delta\nu$, the integration time τ, and the system temperature $T_{\rm sys}$, as given by

$$\sigma_{T_A} = \frac{2T_{\rm sys}(\nu)}{\eta_{\rm spec}\sqrt{n_{\rm pol}\eta_{\rm tel}\Delta\nu\tau}}, \tag{2.13}$$

where $n_{\rm pol}$ is the number of polarizations the telescope uses, and $\eta_{\rm spec}$ and $\eta_{\rm tel}$ are the efficiencies of the spectrograph and the telescope, respectively (for details, see Pety et al. [40]). The factor 2 in the equation appears for observations where position switching is used to reduce noise levels.

Using the definition of the signal-to-noise ratio (SNR) of an observation, we can rearrange Eq. 2.13 to get

$$\tau = \frac{1}{n_{\rm pol}\eta_{\rm tel}}\left(\frac{2}{\eta_{\rm spec}\eta_b}\right)^2 {\rm SNR}^2 \frac{T_{\rm sys}(\nu)^2}{T_R^2\Delta\nu} \tag{2.14}$$

for the observation time, where η_b is the main beam efficiency. For practical uses, the frequency bandwidth of the line can be estimated from the line width in velocity units (ΔV) due to thermal broadening and turbulence, and can be converted into a frequency bandwidth as

$$\Delta\nu = \frac{\Delta V}{c}\nu, \tag{2.15}$$

where ν is the central frequency of the line transition. This conversion is useful as for line transitions ΔV is often reported instead of $\Delta\nu$.

2.3. Level Populations

The intensity of a given molecular line transition is dependent on many factors, including the background radiation field, the transition frequency, and the population of the energy levels. Molecular rotational excitation can happen via two mechanisms: radiative excitation by the background and local radiation fields through the absorption of a photon, and collisional excitation when part of the kinetic or rotational energy of a collisional partner excites the molecule to higher rotational energy levels. The competing processes are radiative and collisional de-excitation, which, combined with the excitation processes, determine the population of a given energy level. The formulation of the theory presented in this section is based on the detailed treatment provided in the book by Tielens [41].

2.3.1 Radiative Excitation

The absorption process that promotes molecules from the lower level l to the upper level u changes the number density of the lower level n_l according to

$$\left(\frac{dn_l}{dt}\right)_{l\to u} = -n_l B_{lu}\bar{J} = -\left(\frac{dn_u}{dt}\right)_{u\to l}, \tag{2.16}$$

where B_{lu} is the Einstein absorption coefficient characterizing the transition probability, $\bar{J}$ is the profile-averaged mean intensity, and the second equality holds in equilibrium. The corresponding emission processes depopulating the upper level–including both spontaneous emission with rate coefficient A_{ul} and stimulated emission with coefficient B_{ul}–are the following:

$$\left(\frac{dn_u}{dt}\right)_{u\to l} = -n_u(A_{ul} + B_{ul}\bar{J}). \tag{2.17}$$

Under equilibrium conditions where the excitation and de-excitation rates balance, we can express the profile-averaged spectral energy density $\bar{J}$ in terms of the Einstein coefficients and level populations as

$$\bar{J} = \frac{A_{ul}}{B_{ul}}\frac{1}{\left(\frac{B_{lu}}{B_{ul}}\frac{n_l}{n_u} - 1\right)} = \frac{2h\nu^3}{c^3}\frac{1}{\left(\frac{g_u}{g_l}\frac{n_l}{n_u} - 1\right)}, \tag{2.18}$$

where g_u and g_l denote the degeneracy of the upper and lower levels, respectively. In a non-LTE system, the level populations can be given by the Boltzmann equation with the definition of the excitation temperature as

$$\frac{n_u}{n_l} = \frac{g_u}{g_l}e^{-h\nu/k_B T_{\rm ex}}, \tag{2.19}$$

which is equivalent to the previous definition that $S_\nu = B_\nu(T_{\rm ex})$.

2.3.2 Collisional Excitation

To include the effect of collisional excitation to reach the final form of the statistical equilibrium equation, we can consider how the level populations can change due to collisions in the ISM. The collision de-excitation rate from the upper energy level to a lower one is given by

$$R_{ul} = n_c\langle\sigma v\rangle_{ul} \equiv n_c k_{ul}, \tag{2.20}$$

where

$$k_{ul} \equiv \int_0^\infty \sigma_{ul}(v) v f_v dv = \sqrt{\frac{8}{\pi\mu(k_B T_{\rm kin})^3}} \int_0^\infty \sigma_{lu}(E) E e^{-E/k_B T_{\rm kin}} dE \tag{2.21}$$

is the collisional de-excitation rate coefficient, n_c is the number density of the collision partner, f_v is the Maxwellian velocity distribution, and μ is the reduced mass of the collisional system. The collisional excitation rate coefficient can be related to the de-excitation rate coefficient via the principle of detailed balance in equilibrium conditions:

$$k_{ul} n_u = k_{lu} n_l \Rightarrow k_{lu} = k_{ul} e^{-h\nu/k_B T_{\rm kin}}. \tag{2.22}$$

Therefore, the rate of change of the population of the lower level due to radiative and collisional excitation is given by

$$\left(\frac{dn_l}{dt}\right)_{l\to u} = -n_l \left(B_{lu}\bar{J} + R_{lu}\right) + n_u \left(A_{ul} + B_{ul}\bar{J} + R_{ul}\right) = -\left(\frac{dn_u}{dt}\right)_{u\to l} \tag{2.23}$$

in equilibrium (see the work of Jansen [42] for details).

To evaluate whether de-excitation is more likely to happen via radiative or collisional processes, we can define a quantity called the critical density, $n_{\rm crit}$. The critical density of a molecule for a given line transition is the number density of the collisional partner at which the collisional de-excitation rate equals the radiative de-excitation rate, which gives

$$n_{\rm crit} \equiv \frac{\sum_{l<u} A_{ul}}{\sum_{l\neq u} k_{ul}}, \tag{2.24}$$

where the sums are over all possible radiative and collisional channels for the transition. As k_{ul} is a temperature–dependent quantity, so is $n_{\rm crit}$, and Eq. 2.24 means that radiative de-excitation only dominates if $n \ll n_{\rm crit}$. The critical density is an important concept in a collisional system, as it helps us to understand how line emission is affected by density for different molecular transitions.

2.3.3 The Escape Probability Method

Solving Eq. 2.23 for statistical equilibrium between the upper and lower levels in a multilevel system is complicated, as the radiation field and the level populations form a coupled system. Therefore, it is often useful to decouple these equations using the so-called escape probability method, which assumes that a fraction of the background radiation field is absorbed by the medium surrounding the source; see the work of Van der Tak et al. [37] for more details. A simple assumption is to write the profile-averaged intensity with the source function as $\bar{J} = (1-\beta)\bar{S}$, where $\bar{S}$ is the profile-averaged source function, and β acts like a measure of probability that a photon can escape the cloud.

Another assumption we can make is that the line profile is very thin around the central frequency, such that it can be approximated by a small rectangle, and hence the profile-averaged source function will approximately equal the source function at the transition frequency ($\bar{S} \approx S_\nu$). This leads to a simplified version of Eq. 2.23 as

$$\left(\frac{dn_l}{dt}\right)_{l\to u} = -n_l R_{ul} + n_u(\beta A_{ul} + R_{lu}) \tag{2.25}$$

for a two-level system, which is independent of the background radiation field. A similar treatment can be implemented for multilevel systems to solve the statistical equilibrium equations.

To determine an explicit value for β, three geometrical models are considered: a static homogeneous sphere, an expanding spherical shell–corresponding to the Sobolev or large velocity gradient (LVG) approximation–and a plane-parallel static homogeneous slab. The corresponding escape probabilities for these models have previously been derived and are given by

$$\beta_{\text{sphere}} = \frac{3}{2\tau_0}\left[1 - \frac{2}{\tau_0^2} + \left(\frac{2}{\tau_0} + \frac{2}{\tau_0^2}\right)e^{-\tau_0}\right] \tag{2.26}$$

for a static homogeneous sphere [43],

$$\beta_{\text{LVG}} = \frac{1 - e^{-\tau_0}}{\tau_0} \tag{2.27}$$

for an expanding spherical shell [44][45], and

$$\beta_{\text{slab}} = \frac{1 - e^{-3\tau_0}}{3\tau_0} \tag{2.28}$$

for a plane-parallel slab [46]. These models require the knowledge of the optical depth τ_0 of the medium at the line frequency, which can be derived from Eq. 2.7 and 2.15, for a homogeneous medium without a global velocity field, assuming a rectangular line profile:

$$\tau_0 = \frac{A_{ul}c^3}{8\pi\nu_{ul}^3}\frac{N_{\text{mol}}}{\Delta V}\left[x_l\frac{g_u}{g_l} - x_u\right], \tag{2.29}$$

where N_{mol} is the column density of the molecule, ΔV is the line width in units of km s^{-1}, and x_l and x_u are the fractional abundances of the lower and upper levels, respectively.

Chapter 3

Methodology & Results

To investigate OCS as a tracer of temperature and density, first, its rotational line intensities were modeled under non-LTE conditions in various environments using `RADEX`, and the resulting outputs were used to identify the lines most likely to be prominent and detectable within certain observational limits. These transitions were then used to constrain the analysis of line intensity ratios over a grid of temperature and density values, allowing for the characterization of the dependency on these parameters. The grid analysis was then applied to real observational data to infer physical conditions across different regions. Finally, based on these findings, an observation plan is proposed for L1157 to further evaluate the practical reliability of OCS as a condition tracer in molecular environments.

3.1. Non-LTE Line Modeling with `RADEX`

To perform `RADEX` simulations for a given molecule, input data must include collisional de-excitation rate coefficients, transition frequencies, and Einstein A-coefficients for spontaneous emission corresponding to each molecular transition. Since `RADEX` is designed to work with molecular data files structured according to the LAMDA database format, the BASECOL-style file containing the updated collisional rate coefficients from Denis-Alpizar et al. [36] was first converted to this format. Following the conversion, the coefficients were rescaled based on Eq. 2.21 using the reduced masses of the He-OCS and H_2-OCS systems as:

$$k_{ul}(\mathrm{H_2} - \mathrm{OCS}) \approx \sqrt{\frac{\mu(\mathrm{He} - \mathrm{OCS})}{\mu(\mathrm{H_2} - \mathrm{OCS})}} k_{ul}(\mathrm{He} - \mathrm{OCS}), \tag{3.1}$$

where $\mu(\mathrm{He} - \mathrm{OCS}) = 3.75$ amu and $\mu(\mathrm{H_2} - \mathrm{OCS}) = 1.95$ amu, leading to a scaling factor of 1.39. After the scaling was applied to the new collisional dataset, both the 1978 and 2023 datasets were used to model the properties of OCS line transitions.

3.1.1 Program Inputs

Obtaining results for the non-LTE excitation of a molecule using `RADEX` requires the user to first define several inputs that model the desired physical conditions. The details of these input parameters are thoroughly described in the work of Van der Tak et al. [37]. Key parameters include the conditions for the astrophysical environment being modeled, including the kinetic temperature T_{kin}, H_2 number density $n_{\mathrm{H_2}}$, molecular column density $N(\mathrm{OCS})$, line width ΔV, background radiation temperature T_{b}, and escape probability model β. For this study, the selected regions

Table 2: Parameter inputs for `RADEX` for the non-LTE OCS line analysis for different astrophysical region models. The research papers used to estimate these values for a given region are referenced below.

Parameter	MC[a,b]	PSE[c,d,e]	GC[f,g]	PPD[c,h,i,j,k] (inner)	PPD (outer)
$T_{\rm kin}$ [K]	20	80	100	500	50
$n_{\rm H_2}$ [cm^{-3}]	10^4	10^6	10^7	10^{10}	10^8
N(OCS) [cm^{-2}]	10^{13}	10^{14}	10^{15}	10^{14}	10^{12}
ΔV [km s^{-1}]	1	5	20	3	0.5
$T_{\rm b}$ [K]	2.73	30	20	50	10
β	$\beta_{\rm sphere}$	$\beta_{\rm LVG}$	$\beta_{\rm LVG}$	$\beta_{\rm slab}$	$\beta_{\rm slab}$

[a]Harada et al. [47]
[b]Goldsmith et al. [48]
[c]Crapsi et al. [49]
[d]Santos et al. [50]
[e]McCutcheon et al. [51]
[f]Ginsburg et al. [52]
[g]Solomon et al. [53]
[h]Nomura et al. [54]
[i]Dutrey et al. [55]
[j]Kutner et al. [56]
[k]Boogert et al. [57]

for which the values were estimated to analyze OCS lines are as follows: molecular cloud (MC), protostellar envelope (PSE), the Galactic Center (GC), and both the inner and outer regions of protoplanetary disks (PPD); the values are presented in Table 2. The model parameters were estimated from previous studies on the physical conditions of various astrophysical objects in the corresponding model regions.

The modeled line transition frequency range for all regions was set to $10 - 500$ GHz based on the collisional rate coefficients available up to $J = 40$ in the new dataset, with an important note that not all line transitions within this spectral range are observable for some of the regions. The most critical inputs for the optical depth calculation, which significantly influence the line intensities, are N(OCS) and ΔV, as shown in Eq. 2.29. Consequently, regions with substantially different physical conditions but similar column density-to-line width ratios may exhibit similar line behavior.

The applied escape probability models were selected based on the anticipated physical conditions in these regions. For the molecular cloud model, a static sphere approximation was used since no significant turbulence and outflows are expected within these regions. In contrast, for the protostellar envelope and the Galactic Center region, an expanding spherical shell model was chosen to represent the effects of stellar outflows and the substantial turbulence resulting in large velocity gradients. For the protoplanetary disk models, the slab model was deemed appropriate, as the large circular rings present in protoplanetary disks can be considered plane-parallel at great distances.

3.1.2 Program Output and Line Analysis

Once the user inputs are provided, the code initiates the iterative calculation of the level populations by making an initial estimate based solely on the background radiation field, i.e, in the optically thin limit. The program's final output is a file that includes key physical parameters for each line transition: the upper state energy $E_{\rm up}$, the excitation temperature $T_{\rm ex}$, the line optical depth τ_0, the Rayleigh-equivalent radiation temperature T_R, as given by Eq. 2.12, and the line flux. Although the Rayleigh–Jeans approximation may not be valid for all transitions, particularly those at higher frequencies, the program still reports the equivalent radiation temperature for all lines to maintain consistency with observationally derived quantities.

The RADEX results for the different model regions, using the input parameters listed in Table 2 for the 1978 and 2023 data, are shown in Fig. 1. Based on the calculated radiation temperatures, certain line transitions are expected to be more prominent due to the substantial variation in environmental conditions. For example, energy levels with $J_u \gtrsim 15$ are not significantly excited in the molecular cloud model; the most prominent lines are expected to have J_u below this value.

In contrast, OCS in protostellar envelopes, Galactic Center regions, and the outer regions of protoplanetary disks exhibit significant excitation across the full range of J_u and the frequency values considered. Transitions with $J_u > 20$ become increasingly dominant in the warmest environments, particularly in the inner regions of protoplanetary disks.

The modeled radiation temperatures vary between approximately 10^{-4} K and 0.5 K for the PSE, GC, and PPD models for both collisional datasets, while for the MC model it drops to approximately 10^{-14} K after dropping below 10^{-4} K at $J_u \approx 20$. Within practical observational limits, transitions with equivalent radiation temperatures as low as $10^{-4} - 10^{-3}$ K can be observed by some radio telescopes; the detectability of these lines is explored in detail in section 3.1.4 for all regions considered. Among the five models, the lowest intensities are generally observed in the outer regions of protoplanetary disks, for which the modeled temperatures remain below 10^{-2} K.

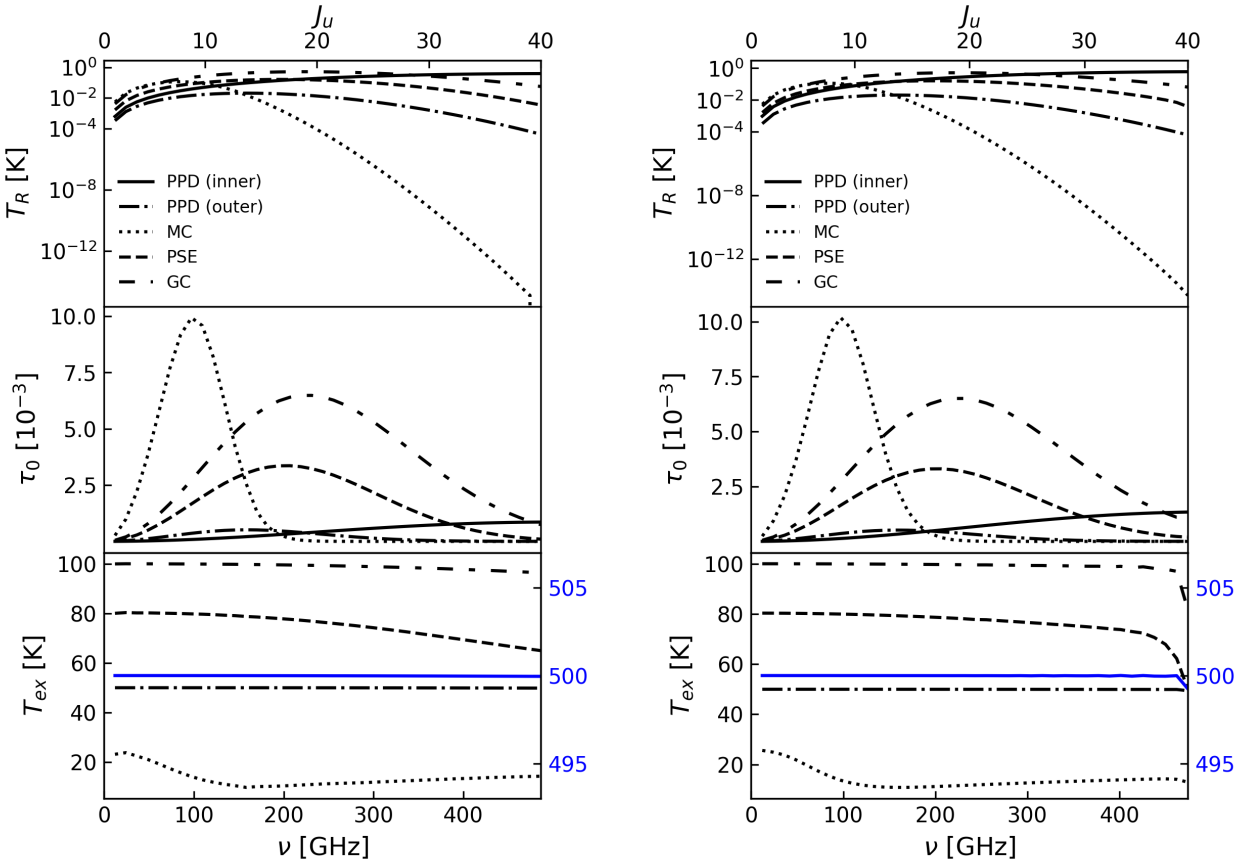

(a): 1978 data

(b): 2023 data

Figure 1: Figure (a) shows the radiation temperature (upper panel), opacity (central panel), and excitation temperature (lower panel) of the line transition described by the upper J level and the corresponding frequency ν for the 5 different regions considered using the 1978 collisional data. Figure (b) shows the same line properties for the 2023 collisional data. The blue colour used for the excitation temperature is for the inner PPD model.

This is mainly due to the low molecular column density of 10^{12} cm^{-2} in this model, which leads to a corresponding decrease in line intensities. Furthermore, protoplanetary disks are generally very dense environments, with the modeled densities of 10^8 cm^{-3} and 10^{10} cm^{-3} for the outer and inner regions respectively, exceeding the critical density of all line transitions considered. This means that collisional de-excitation is favored over radiative processes, significantly reducing the line intensity and, consequently, the equivalent radiation temperature.

The inner regions, however, exhibit the opposite behavior: OCS lines with $J_\mathrm{u} \gtrsim 20$ are expected to be prominent in the central regions of protoplanetary disks despite the high density, with radiation temperatures reaching above 0.1 K. This is likely caused by the significantly stronger background radiation considered, which increases radiative excitation for higher-level transitions.

The Galactic Center model exhibits excitation of nearly all transitions with radiation temperatures greater than 10^{-2} K, indicating the strong detectability of OCS in such regions. The high molecular line intensities predicted for this model result from the combined effects of a large column density of 10^{15} cm^{-2}, high kinetic temperature of 100 K, and strong background radiation with equivalent blackbody temperature of 20 K. The similarity between the line behavior in the Galactic Center and protostellar envelope models arises from comparable column density-to-line width ratios, background radiation temperatures, and kinetic temperatures. The comparatively lower radiation temperatures modeled for the protostellar envelope are likely attributable to its reduced molecular column density and H_2 number density.

The line optical depth τ_0 depends on both the properties of the astrophysical environment and the characteristics of the specific line transition, as described by Eq. 2.29. This makes its connection to the radiation temperature somewhat complicated. Since $\tau_0 \ll 1$ in all cases for the line transitions considered in Fig. 1, radiative trapping can be assumed to be negligible. The opposite behavior of the optical depth between the molecular cloud and the inner protoplanetary disk models–i.e., relatively low T_R but higher τ_0 in the MC model, and the reverse in the inner PPD model–can be explained by Eq. 2.10, which is particularly sensitive to small values of τ_0. Even a modest increase in optical depth in the optically thin regime can significantly reduce the line intensity, as seen in the MC case. Conversely, the lower optical depth in the inner PPD allows for stronger line emission. If both optical depths were much larger, the factor $(1-e^{-\tau_0})$ in Eq. 2.10 would approach unity in both cases, and the lines would be optically thick. In that regime, the intensity would depend primarily on the excitation temperature rather than on the optical depth.

The excitation temperature is useful for quantitatively assessing how close the physical conditions in different regions are to the LTE conditions. For transitions with $J_\mathrm{u} \lesssim 35$ for the 2023 dataset, the GC, PSE, and PPD models show that the excitation and kinetic temperatures are almost the same, which is not the case for the MC model. This emphasizes that non-LTE conditions and modeling are most important for this region.

3.1.3 The 2023 vs. 1978 Datasets

To compare the 2023 and 1978 collisional datasets used for the line modeling, the absolute and relative differences for the modeled line properties were calculated and are shown in Fig. 2. The most significant differences between the modeled radiation temperatures and optical depths were observed in the MC and inner PPD models. The new collisional data predict significantly higher values for both parameters for the MC model, with ΔT_R and $\Delta\tau_0$ reaching values above 0.2 K and 4×10^{-4} for transitions with $J_\mathrm{u} \gtrsim 35$, with differences increasing at higher frequencies. For the optical depth, this is likely due to its small absolute value for higher-lying transitions, which can lead to significant differences more easily.

Relative differences in excitation temperature values are more substantial for higher-lying transitions with $J_{\rm u} \gtrsim 35$, which was also expected from Fig. 1, where excitation temperatures drop by 10-20% at frequencies above 400 GHz. An excitation temperature lower than the kinetic temperature indicates that the level population is lower than expected under LTE conditions, implying that these transitions are more difficult to populate through collisional and radiative processes. This effect is particularly pronounced for the molecular cloud model, where the excitation temperature remains below the kinetic temperature for most line transitions. In contrast, only the outer protoplanetary disk region model exhibits an excitation temperature that remains nearly constant across the entire frequency range considered, indicating that conditions in such regions are close to thermal equilibrium and that line transitions generally follow LTE behavior.

The fact that the excitation temperatures are significantly lower than the kinetic temperature by up to 15 K in most regions for transitions with $J_{\rm u} \gtrsim 35$ means that the new collisional data, which include proper quantum mechanical calculations, suggest these levels are harder to populate through collisional excitation than previously expected. This is likely because collisional cross sections are sensitive to fine details of the potential energy surface (PES) of the system. It is therefore expected that the older model may have used simplified PES or averaged interaction potentials that overestimated the coupling to high-J levels.

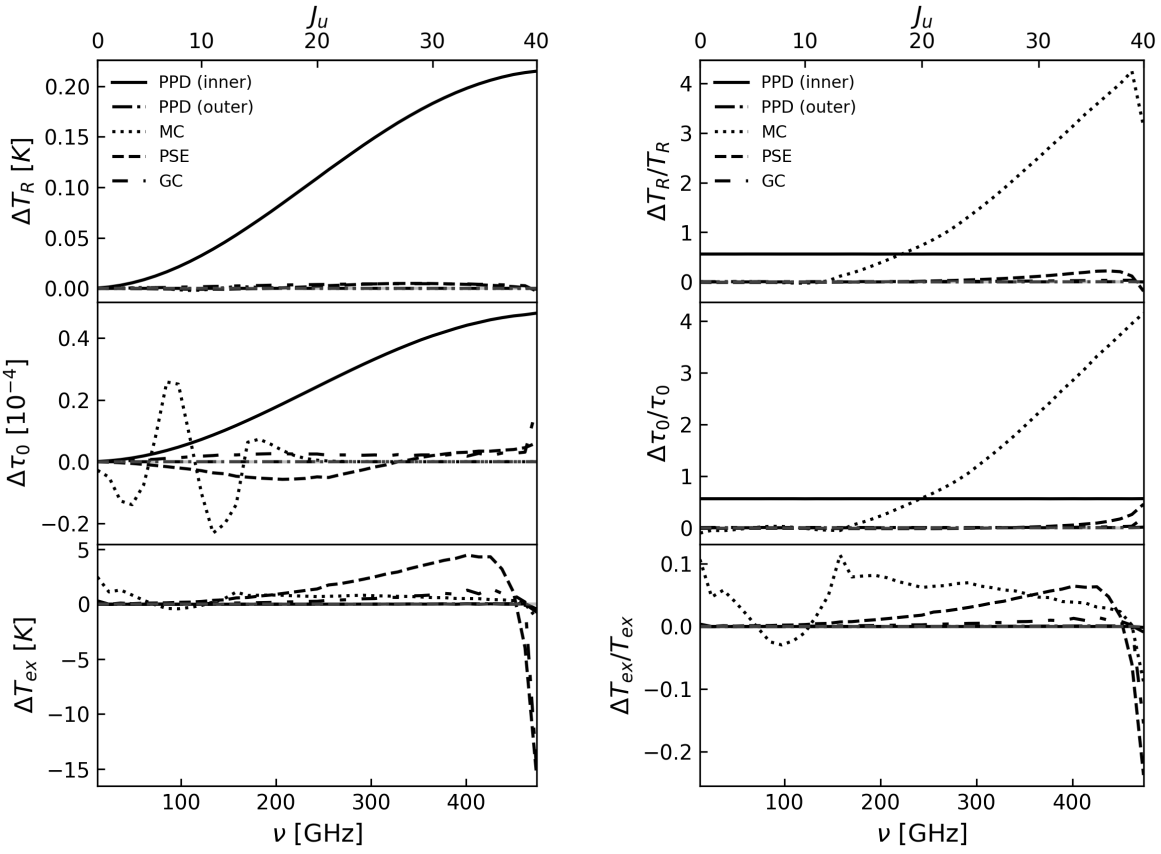

(a) (b)

Figure 2: Figure (a) shows the absolute difference between the radiation temperature (upper panel), optical depth (central panel), and excitation temperature (lower panel) for the 5 different regions considered for the 1978 and 2023 data. Figure (b) shows the relative difference between the 1978 and the 2023 collisional data for the same parameters.

The differences in the collisional de-excitation rate coefficients not only lead to changes in the modeled line properties but also affect the critical densities of the line transitions. This is important because the critical density is a key concept that constrains the usability of molecular lines for density tracing: if the density of the collisional partner significantly exceeds $n_{\rm crit}$, the line intensities become independent of density. The critical densities of several transitions were calculated using both the old and new collisional data at some temperatures; the results are presented in Table 3.

Table 3: Calculated critical densities for various OCS rotational line transitions at selected temperatures for the 1978 and 2023 datasets.

Transition	$n_{\rm crit}[{\rm cm}^{-3}]$: 1978 data			$n_{\rm crit}[{\rm cm}^{-3}]$: 2023 data		
	10 K	40 K	80 K	10 K	40 K	80 K
$2 \rightarrow 1$	9.2×10^1	1.1×10^2	1.1×10^2	1.3×10^2	2.1×10^2	2.1×10^2
$10 \rightarrow 9$	5.4×10^4	4.5×10^4	4.6×10^4	5.1×10^4	5.8×10^4	6.0×10^4
$20 \rightarrow 19$	5.0×10^5	4.8×10^5	4.6×10^5	5.0×10^5	5.4×10^5	5.6×10^5
$30 \rightarrow 29$	1.9×10^6	1.7×10^6	1.6×10^6	1.9×10^6	1.9×10^6	2.0×10^6
$40 \rightarrow 39$	5.1×10^6	4.2×10^6	4.0×10^6	5.0×10^6	4.9×10^6	5.0×10^6

The critical densities of most transitions with $J_{\rm u} \gtrsim 20$ seem to slightly decrease with temperature for the 1978 dataset, while an opposite trend is observed for the 2023 one. Even though these values are dependent on temperature, they remain the same order of magnitude for temperatures up to 80 K. Beyond this temperature, the critical densities were only calculated for the 1978 data (see the critical densities in Table 12 in Appendix A) due to the lack of available collisional rate coefficients for the 2023 data. However, it is expected that for all temperature ranges considered in this study (up to 500 K) the critical densities remain within the same order of magnitude based on the extrapolated rate coefficients by Schöier et al. [33] for the 1978 dataset, which should still indicate relatively accurate values even for the 2023 data. This means that the line intensity ratios for the temperature–density diagnostics should behave quite accurately for all region models. As the critical densities of the $J = 40 \rightarrow 39$ transition vary around 5×10^6 cm^{-3}, we can expect line intensities to saturate for densities significantly above this value, therefore mainly for the PPD models.

3.1.4 Line Detectabilities

Based on the modeled radiation temperatures, the most prominent molecular lines for observational purposes were estimated using Eq. 2.13, which accounts for the characteristics and efficiencies of the telescopes in question. To assess the detectability of these lines, a selection of current and upcoming radio telescopes–including the Next Generation Very Large Array (ngVLA)–was considered; see Table 4.

The two key telescope-specific parameters that influence detectability are the system temperature and the main beam efficiency, both of which are frequency dependent. Since the frequency dependence is rather hard to accurately model, a conservative approach was taken: a lower estimate of the telescope efficiency (based on the aperture efficiency) and an approximate system temperature value were adopted across the full operating frequency range of each telescope. This ensures that the number of potentially detectable lines is not overestimated due to overly optimistic assumptions.

Table 4: Properties of current and future telescopes used in the detectability analysis.

Telescope	Freq. [GHz]	η_{tel}	T_{sys} [K]	Ref.
GBT	0.3–115	0.6	100	[58]
ALMA	84–950	0.8	100	[59][60]
NOEMA	80–370	0.5	120	[61][62]
ngVLA	1–115	0.8	30	[63]

In addition to the unique characteristics of each telescope, several parameters were uniformly applied across all instruments in the detectability analysis to ensure consistency. These include a spectral efficiency of 0.8, a main beam efficiency of 0.75, a SNR requirement of 10, two polarizations, and a maximum integration time of 48 hours. These values reflect typical observational configurations and performance expectations, providing an approximate but realistic basis for comparison among both current and upcoming telescopes for OCS line transition detection.

Although the spectral, telescope, and main beam efficiencies can vary between instruments, these values are not expected to constitute significant differences in the estimated detectable line transition ranges, making them reasonable approximations for this analysis. Using these standardized parameters, the most prominent lines in each region were identified, which guided the selection of line transitions suitable for temperature and density diagnostics.

Using the calculated radiation temperatures and Eq. 2.14, the most prominent line transitions for different telescopes were estimated, as summarized in Table 5. Overall, the MC and outer PPD models appear to be the most limited in terms of OCS line detectability. For the molecular cloud model, easily detectable transitions are expected to lie within the range $J_{\mathrm{u}} = 2{-}14$, while for the outer disk model, transitions around $J_{\mathrm{u}} = 5{-}21$ are likely to be observable with current (or future) telescopes.

For the molecular cloud model, transitions with $J_{\mathrm{u}} > 14$ are unlikely to be useful for astrophysical diagnostics, as they are expected to be undetectable within practical observational time frames. In contrast, for the protostellar envelope and the Galactic Center, the broader line widths–and thus higher intensities–enable the detection of most transitions up to $J_{\mathrm{u}} = 40$ within the studied frequency range using ALMA, and transitions with $J_{\mathrm{u}} < 10$ remain accessible also with GBT. For the inner PPD model, it is also expected that most OCS line transitions are observable with current operating telescopes. The transition ranges in Table 5 were further investigated for temperature–density diagnostics.

Table 5: Detectable transitions with J_{u} ranges for different environments using current and future telescopes.

Telescope	MC	PSE	GC	PPD (inner)	PPD (outer)
GBT	3–9	3–9	2–9	5–9	–
ALMA	7–14	7–40	7–40	7–40	9–21
NOEMA	7–13	7–30	7–30	7–30	12–17
ngVLA	2–9	2–9	1–9	3–9	5–9
Overall	2–14	2–40	1–40	3–40	5–21

3.2. Line Ratio Behavior Across Temperature–Density Grids

For temperature and density diagnostics, a new Python script `radex_grid.py` was developed (see Appendix D for the code). The user inputs for this script were designed to match those of `RADEX` to construct a temperature–density grid for line transition ratios. To achieve this, additional input parameters can be defined for the maximum and minimum temperature and density, along with the number of grid points n for each parameter. This setup allows for the definition of a range for both the kinetic temperature and H_2 number density. The script executes `RADEX` n^2 times–once for every unique temperature–density pair–calculating the molecular line transition intensities in the standard manner. The resulting output files (n^2, equivalent to those of `RADEX`) are then used to compute the line transition ratios for each point in the grid, which serve as diagnostic tools by enabling the determination of the kinetic temperature and density by identifying their intercepts. For consistency, the same input parameters were applied in all astrophysical regions as given in Table 2, with the specific temperature and density ranges summarized in Table 6.

Table 6: Kinetic temperature and H_2 number density ranges used for the grid analysis of OCS line transition ratios for the different environment models.

Parameter	MC[a,b,c]	PSE[d]	GC[e]	PPD[f] (inner)	PPD (outer)
$T_{\rm kin}$ [K]	5–30	10–300	30–200	100–500	5–100
$n_{\rm H_2}$ [cm^{-3}]	10^2–10^6	10^4–10^8	10^4–10^7	10^8–10^{12}	10^6–10^{10}

[a]Vázquez-Semadeni et al. [64] [b]Loren et al. [65] [c]Rowan-Robinson [66] [d]Takakuwa et al. [67] [e]Ginsburg et al. [68] [f]Nomura et al. [69]

To analyze the behavior of line transition ratios in models of different astrophysical environments, $n = 100$ was selected to ensure that the resolution is high enough such that the uncertainties corresponding to unique combinations of temperature and density for a given line ratio contour line are minimized. Then, the pixel-wise distances between the ratio images were calculated to identify those six (for each region) that exhibit the most distinct line behavior relative to each other. Subsequently, contours for all regions were plotted for different transition ratios at levels of 20%, 40%, 60%, and 80% relative to the maximum visible value.

3.2.1 Molecular Cloud

For the molecular cloud model, the six line transition ratios exhibiting the most distinct behavior across the specified temperature–density grid are shown in Fig. 3. The most notable characteristic of this region, based on the line transition ratios, is that in low-density regions with $n_{\rm H_2} \lesssim 10^4$ cm^{-3}, the ratios are highly sensitive to changes in density, whereas in high-density regions with $n_{\rm H_2} > 10^4$ cm^{-3}, the contour values primarily respond to variations in the kinetic temperature of the cloud. This suggests that the model effectively traces the line-ratio behavior around the critical density of the transitions. Specifically, for lines in regions with $n_{\rm H_2} \gg n_{\rm crit}$, collisional de-excitation dominates over radiative de-excitation, which depends mainly on the kinetic temperature through the collisional de-excitation rate coefficient. Conversely, in regions where $n_{\rm H_2} \ll n_{\rm crit}$, collisional de-excitation is less significant, so even subtle changes in density can cause substantial differences in line intensities and their ratios.

We can also see that, where the critical density of the transitions is not yet reached, the line transition ratios increase with density. This is especially clear for the $4 \rightarrow 3/3 \rightarrow 2$ and $4 \rightarrow 3/2 \rightarrow 1$ ratios, where the contour lines are almost vertical for $n_{\rm H_2} < 10^4$ cm^{-3}. As the

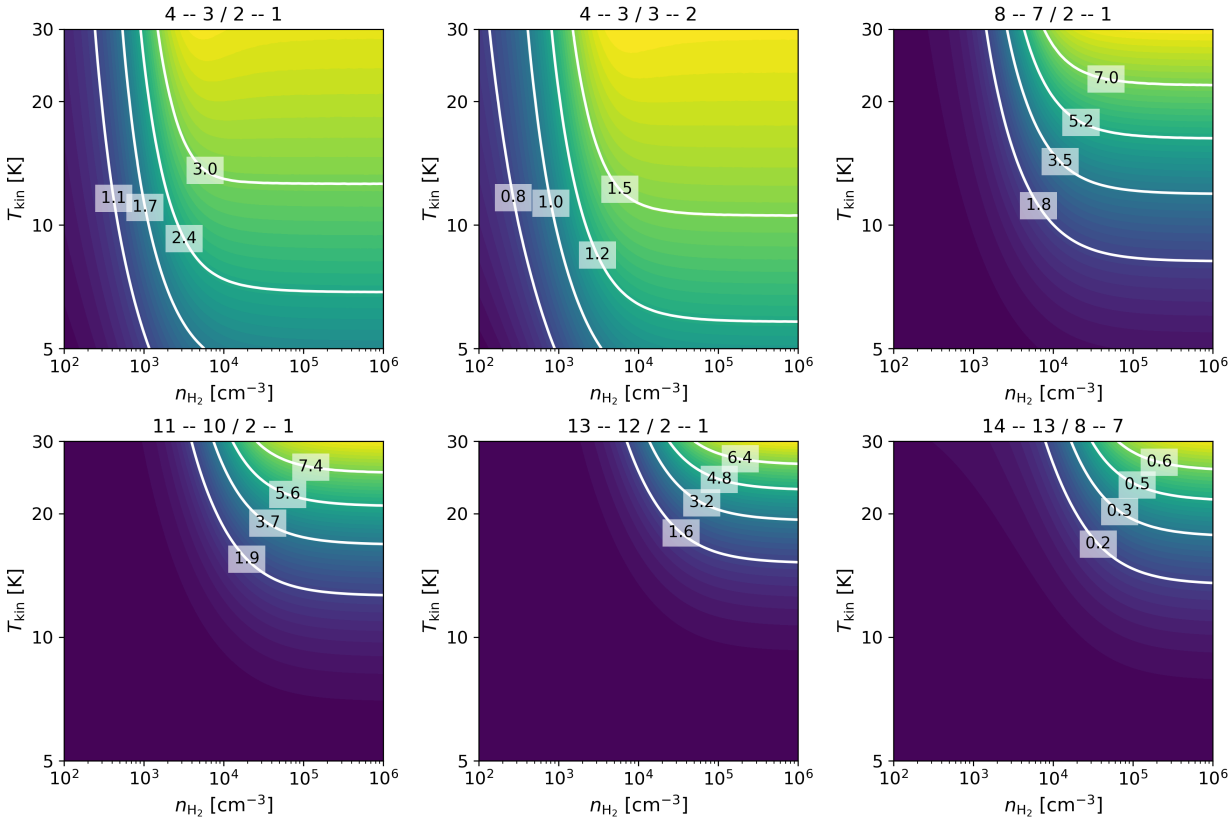

Figure 3: The six most distinct line transition ratio patterns across the modeled temperature–density map for the molecular cloud model within the range of the expected most prominent transitions.

density increases, the frequency of collisions rises, leading to greater population differences and causing the line-ratio values to begin increasing below the critical density.

For this model, the line ratios appear to peak at the ratio of $11 \rightarrow 10/2 \rightarrow 1$ with values reaching up to around 8. Ratios involving transitions with higher J_u start to have lower and lower values, which is especially prominent for the $14 \rightarrow 13/8 \rightarrow 7$ line combination, having values below unity for the entire analyzed grid. This trend can be explained by looking at the behavior of the radiation temperature of the transitions for the MC regions in Fig. 1, which peaks around $J_u = 9$, and decreases rapidly for higher values.

For ratios involving low-lying transitions, the line transition ratios peak at a given density at temperatures above around 15 K, after which the ratios decrease. For example, the $4 \rightarrow 3/2 \rightarrow 1$ ratio reaches a maximum around 5×10^3 cm^{-3} for temperatures above 15 K and then decreases with increasing density. The underlying reason for this is that higher-J transitions generally possess higher critical densities, causing collisional de-excitation to dominate at higher densities. As the density reaches the critical density, the intensity of the higher-J line begins to drop rapidly as collisional de-excitation becomes dominant. If this decline occurs more dramatically than for the lower-J transition–which is expected due to the higher critical density–then the resulting line ratio decreases accordingly, leading to a peak for the ratio at a given density. This happens only above a given temperature threshold because the upper energy level has to be sufficiently populated for this peak to occur.

Beyond the critical densities of line transitions where line intensities become primarily dependent on temperature, the line ratio values eventually level off at higher and higher densities for

transitions with higher $J_{\rm u}$ values. This shift in the plateau occurs because the critical density increases with $J_{\rm u}$, as transitions take place at higher frequencies that increase the Einstein A_{ul} coefficient for spontaneous emission. Consequently, the densities at which these line ratios flatten shift to higher values. This effect is clearly visible across the six panels in the referenced figure.

3.2.2 Protostellar Envelope

The contours of the calculated OCS line ratios behave quite similarly for the protostellar envelope model shown in Fig. 4. For regions with $n_{\rm H_2} \lesssim 10^6$ cm^{-3}, most line ratios increase with increasing density until the critical densities of the transitions are reached, after which the values are essentially only affected by the kinetic temperature. We can also see that transitions that lie far apart energetically from each other, such as the $22 \rightarrow 21$ and $2 \rightarrow 1$ transitions, result in stronger diagnostic power, as these line ratios can reach values up to $\sim 50 - 60$, which makes it significantly more useful than closely lying ones such as the $10 \rightarrow 9$ and $9 \rightarrow 8$ transitions.

For the $20 \rightarrow 19/19 \rightarrow 18$ ratio, we can see that below a threshold kinetic temperature of around 30 K, the line transition ratios exhibit the opposite behavior: their values decrease with the increase of density. Although this behavior is only clearly visible for one of the ratios presented for this model, other line transition combinations also had a similar behavior. This is likely due to the strong background radiation field with an equivalent blackbody temperature of 30 K, which affects different molecular lines differently. Below $T_{\rm kin} \sim 30$ K, the energy distribution of the molecules is likely such that most of them do not have enough kinetic energy to excite many other

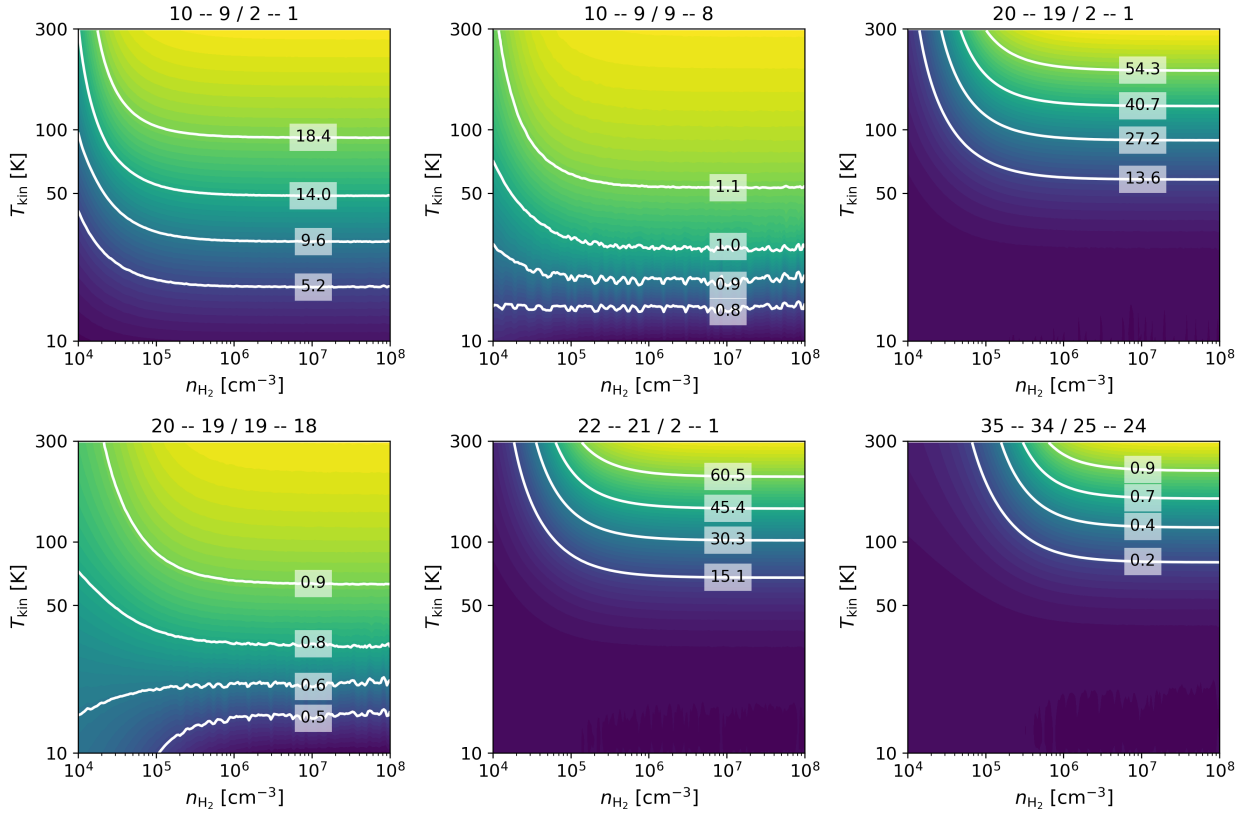

Figure 4: The six most distinct line transition ratio patterns across the modeled temperature–density map for the protostellar envelope model within the range of the expected most prominent transitions.

molecules collisionally. Thus, radiative excitation by the background radiation field dominates the excitation processes.

For a blackbody temperature of 30 K, the frequency at which the maximum intensity occurs is $\nu \approx 1800\,\mathrm{GHz}$, which is significantly higher than the frequency range of $10 - 500\,\mathrm{GHz}$ analyzed. As higher line transitions occur at higher frequencies, this background radiation field favors radiative excitation for transitions with higher J_u. This means that, in low-temperature regions, the line-transition ratios decrease with increasing density because the lower-lying transition is more strongly influenced by collisional excitation than by radiative processes. As a result, its intensity increases, which lowers the ratio as the density increases. This behavior becomes negligible at higher temperatures as collisional excitation starts to dominate for higher energies, and we recover the usual line-transition behavior also found for the MC model.

Another contribution leading to the same results is that, as higher-level transitions have higher critical densities, radiative de-excitation dominates collisional de-excitation, meaning that these transitions will have higher intensities. As the density increases, collisional de-excitation starts to balance radiative excitation, which leads to a balance in the line ratio values (as the lower transition is more dominated by collisional de-excitation than radiative one for the same densities), and the level populations become independent of the kinetic temperature.

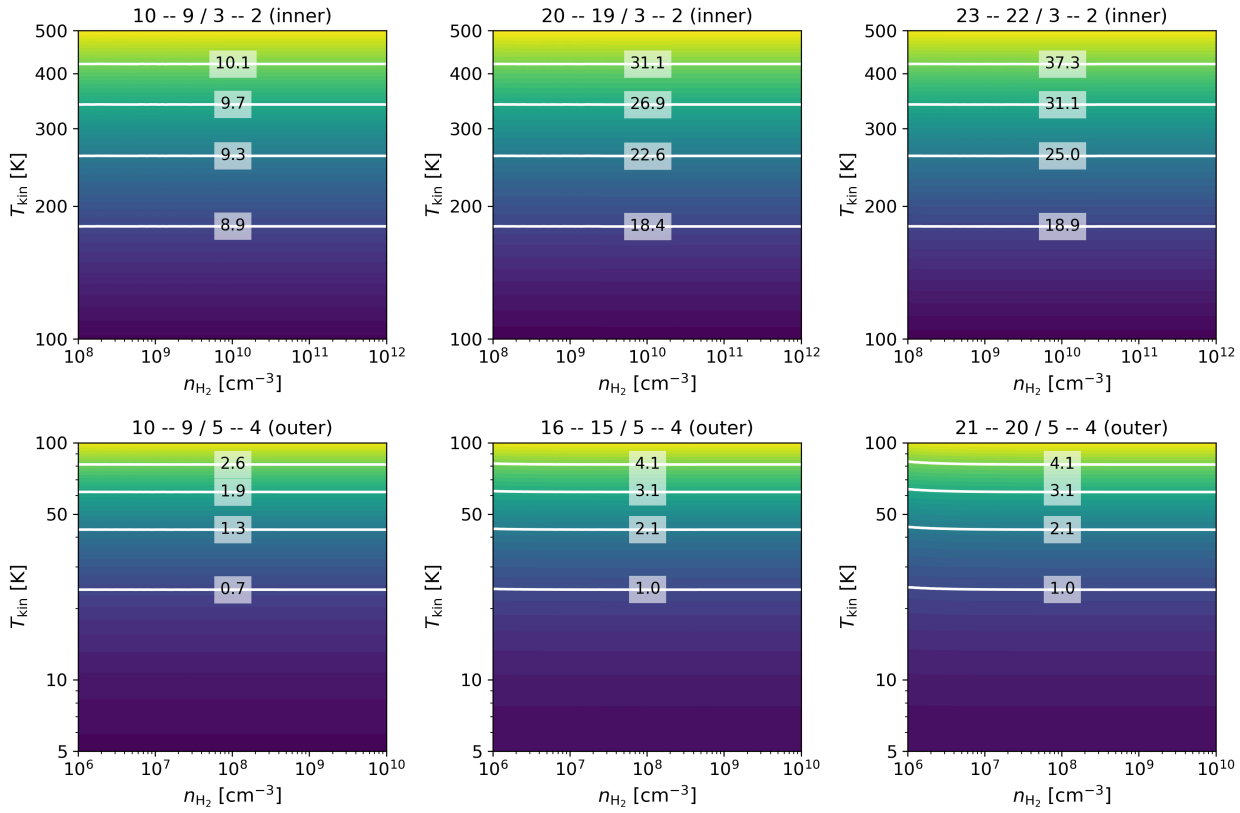

Figure 5: The six most distinct line transition ratio patterns across the modeled temperature–density map for the protoplanetary disk model (3-3 for both inner and outer regions) within the range of the expected most prominent transitions.

3.2.3 Protoplanetary Disk

Generally, protoplanetary disks have significantly higher densities compared to the other regions considered in this study. As a result, the densities lie well above the critical densities of the analyzed line transitions, even for the $J = 40 \rightarrow 39$ transition. Under these conditions, the intensities of the transitions become insensitive to changes in density and instead depend primarily on temperature. This behavior can be clearly observed in Fig. 5, where both the inner and outer regions of the disk show minimal variation in line ratios with density. Consequently, OCS transitions are not suitable for tracing density in high-density environments such as protoplanetary disks, as they primarily respond to changes in temperature.

3.2.4 Galactic Center

The OCS line ratio contours for the GC model can be seen in Fig. 6. The line ratio behavior for this model is similar to that of the molecular cloud and protostellar envelope models. This similarity can be attributed to the fact that the density ranges for which the line transitions are modeled and the molecular column density-to-line width ratios of these models are fairly similar. The latter determines the opacity and hence the line intensity, which explains the similarities between the two models. Below the critical densities at a given temperature, the line ratios increase with density, which can again be attributed to the fact that molecules with higher kinetic energies favor excitation to higher energy levels. This causes an increase in the population for higher energy levels, leading to higher ratio values for higher densities.

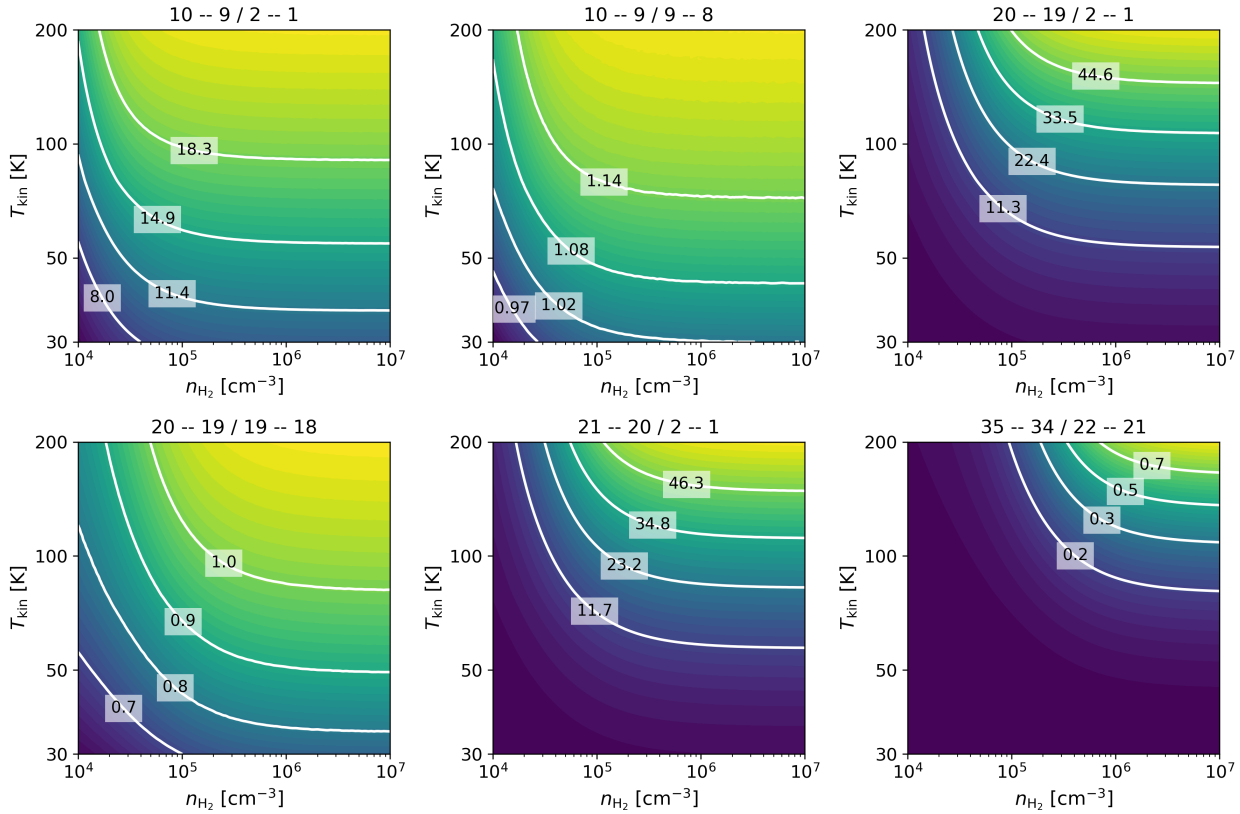

Figure 6: The six most distinct line transition ratio patterns across the modeled temperature–density map for the Galactic Center model within the range of the expected most prominent transitions.

A significant difference between the Galactic Center and the molecular cloud model is not the general behavior but the values of the line transition ratio contours. For example, the $11 \rightarrow 10/2 \rightarrow 1$ line ratio has a value of around 7.4 for the 80% contour line for the molecular cloud model, while the $11 \rightarrow 10/2 \rightarrow 1$ transition (similar enough for comparison) has a value of 14.9 for the same contour. The generally higher ratio values can be explained by the significantly larger line width for the GC model, which was chosen because of the turbulent properties of the region.

3.3. Temperature–Density Diagnostics

For environmental diagnostics, real observational data with reported antenna temperatures are required. If molecular lines are observed with the same telescope, the ratios of antenna temperatures correspond directly to the radiation temperature ratios used in the models. By plotting these ratios as contour lines on the temperature–density grids, intersections of the contours can be identified to constrain the physical conditions of the environment. It is important to note that different line transitions are affected differently by the input parameters; therefore, linear combinations of the same line ratios might lead to different results.

To apply this approach using `radex_grid.py`, observational data of OCS transitions–including antenna temperatures and intensities–were used for Sagittarius B2, DM Tau, and the ridge, plateau, and core regions of Orion KL. These observations were analyzed through the MC, outer PPD, PSE, and Galactic Center models. The Galactic Center model is particularly suitable for the Orion KL plateau due to its ability to represent the large linewidths caused by turbulence from massive star formation, even though Orion KL does not lie close to the Galactic Center. By calculating the ratios of reported antenna temperatures for different line transitions and mapping these onto the modeled temperature–density grids, the intersecting contour lines provide approximate constraints on the temperature and density ranges in these astrophysical environments.

3.3.1 Sagittarius B2

The first region considered is near the Galactic Center in the Milky Way, specifically the Sagittarius B2 giant molecular cloud. Therefore, the analysis for this region utilized the molecular cloud model previously analyzed. Although this cloud is part of the Galactic Center, its conditions are better represented by the MC model than the GC model, primarily due to the temperature ranges considered.

To constrain the environmental conditions for this region, observed OCS lines and their measured antenna temperatures were used as reported by Goldsmith et al. [48], see Table 7. Various combinations of observed line transitions were analyzed, however, not all combinations of line transition ratios had intercepts at a given temperature and density combination.

Table 7: OCS transitions and their reported antenna temperatures from Goldsmith et al. [48] measured in Sagittarius B2 using the Five College Radio Astronomy Observatory.

Transition	T_A [K]
$7 \rightarrow 6$	0.70 ± 0.2
$8 \rightarrow 7$	0.85 ± 0.15
$9 \rightarrow 8$	0.70 ± 0.15
$12 \rightarrow 11$	0.45 ± 0.2

The combinations that yielded results are presented in Table 8, along with the corresponding approximate temperatures and H_2 number densities (see Fig. 10 for the plots in Appendix B). The fact that not all ratio combinations led to intercepts was expected from the non-LTE analysis of the line behavior. Since excitation temperatures are neither constant nor equal to the kinetic temperature of the gas, not all combinations of line transition ratios correspond to the same parameters. The models also assume isothermal and homogeneous conditions, which are rarely met in practice. Sagittarius B2 is a highly turbulent molecular cloud, implying significant variations in density and temperature.

Table 8: Identified line transition ratio intercepts for Sagittarius B2 and the corresponding modeled kinetic temperature and H_2 number density values.

Line transition ratios	T_{kin} [K]	$n_{\mathrm{H_2}}$ [cm^{-3}]
$12 \rightarrow 11/7 \rightarrow 6$ & $12 \rightarrow 11/9 \rightarrow 8$	$\sim$20	$\sim 10^5$
$12 \rightarrow 11/7 \rightarrow 6$ & $9 \rightarrow 8/7 \rightarrow 6$	$\sim$20	$\sim 10^5$
$12 \rightarrow 11/8 \rightarrow 7$ & $9 \rightarrow 8/7 \rightarrow 6$	$\sim$30	$\sim 10^4$
$12 \rightarrow 11/9 \rightarrow 8$ & $9 \rightarrow 8/7 \rightarrow 6$	$\sim$20	$\sim 10^5$

The strong agreement between the derived temperature and density values suggests that the observed OCS transitions likely probe similar regions within the cloud. Furthermore, the reliability of these values depends on the local density being comparable to the critical densities of the transitions. The inferred density for Sagittarius B2 is close to the critical densities of the relevant transitions (see Table 3 for all values in Appendix A), indicating that the corresponding line ratios are well-suited for constraining both temperature and density in this region.

This interpretation is consistent with the similarity of the derived physical parameters. Thus, we conclude that the region of Sagittarius B2 probed by the observed OCS transitions is characterized by a kinetic temperature of $T_{\mathrm{kin}} \approx 20 - 30$ K and a molecular hydrogen density of $n_{\mathrm{H_2}} \approx 10^4 - 10^5$ cm^{-3}. These values are in fairly good agreement with the cold and dilute regions within the molecular cloud, which have $T_{\mathrm{kin}} \approx 20 - 60$ K and $n_{\mathrm{H_2}} \approx 10^4 - 10^6$ cm^{-3} [70][71].

3.3.2 Orion KL

Orion KL is a well-known star-forming region characterized by active chemistry and a rich molecular inventory [72]. Numerous molecular species have been detected in this region, including OCS, for which a relatively large number of antenna temperatures have been reported by Tercero et al. [73] (see Table 9). These observations were used to estimate the physical conditions in the ridge, plateau, and hot core components of the nebula. The ridge typically refers to a dense, elongated structure within the molecular cloud, commonly associated with regions of active star formation and high turbulence. In contrast, the plateau encompasses a broader and more extended region, often featuring a flatter density profile and including material outflowing from embedded young stellar objects. The hot core refers to the hottest and densest central regions of Orion KL.

For the ridge component, the protostellar envelope model was adopted, as it is representative of turbulent star-forming regions. The observed OCS line transitions produced multiple line intensity ratios, leading to intercepts on the modeled temperature–density grid, as shown in Fig. 7 (a). Out of approximately 3000 possible line ratio combinations, around 80 produced valid intersecting solutions. The physical conditions derived from these intercepts indicate a temperature range of $T_{\mathrm{kin}} \approx 60 - 200$ K and a H_2 number density range of $n_{\mathrm{H_2}} \approx 10^4 - 10^6$ cm^{-3}. Most of the

Table 9: Measured OCS line transition antenna temperatures in Orion KL from Gaussian fits reported by Tercero et al. [73] using the IRAM 30m telescope.

Transition	Ridge T_A [K]	Plateau T_A [K]	Hot Core T_A [K]
$7 \rightarrow 6$	2.30	0.49	1.02
$8 \rightarrow 7$	3.56	0.85	1.68
$9 \rightarrow 8$	3.85	1.08	2.29
$11 \rightarrow 10$	4.36	1.80	2.53
$12 \rightarrow 11$	6.63	3.29	2.82
$13 \rightarrow 12$	5.32	2.67	4.16
$14 \rightarrow 13$	3.70	-	-
$17 \rightarrow 16$	4.18	2.83	5.83
$18 \rightarrow 17$	4.47	3.06	4.77
$19 \rightarrow 18$	3.57	4.39	6.14
$20 \rightarrow 19$	3.24	2.75	5.10
$21 \rightarrow 20$	4.68	1.46	2.99
$23 \rightarrow 22$	4.34	3.09	2.62

solutions cluster within $T_{\text{kin}} \approx 60 - 120\,\text{K}$ and $n_{\text{H}_2} \approx 10^5 - 10^6\,\text{cm}^{-3}$, which is consistent with previous studies of Orion KL, which report a temperature range of $T_{\text{kin}} \approx 50 - 300\,\text{K}$, and $n_{\text{H}_2} \approx 10^5 - 10^6\,\text{cm}^{-3}$ [74][75].

A particularly notable aspect of this region is the observed trend in which specific line transitions are more effective for diagnosing environmental conditions. As illustrated in Fig. 7 (a), several prominent transitions have been highlighted. Among these, the $J = 7 \rightarrow 6$ transition seems to be the most diagnostically valuable, appearing in the upper level of around 40 distinct combinations of line intensity ratios.

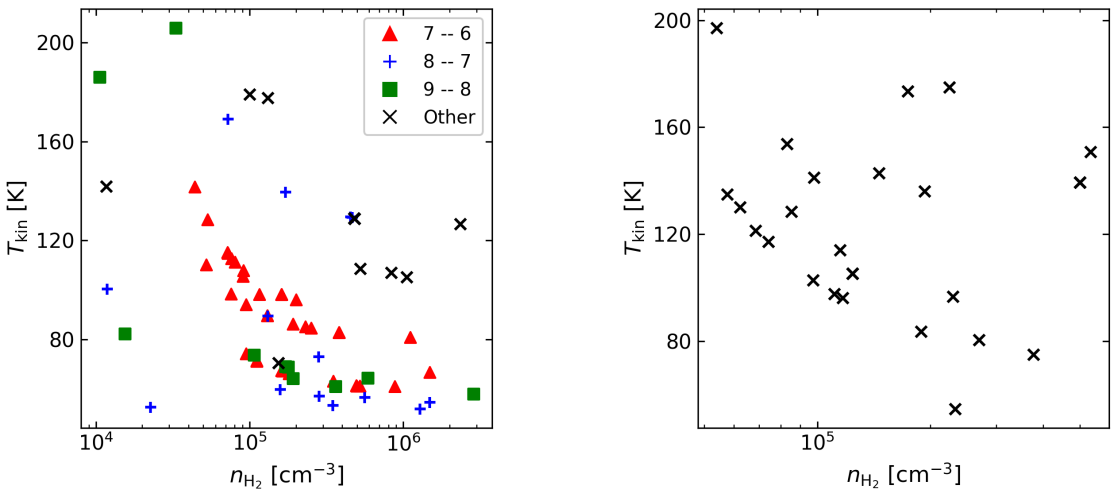

Figure 7: Found line ratio intercepts for the Orion KL ridge (a) and plateau (b) regions based on the antenna temperatures reported by Tercero et al. [73]. Specific transitions that led to a relatively high number of intercepts for the ridge region are marked with colours.

It is also important to note that no transition ratio combinations are found to trace densities significantly exceeding $10^6\,\mathrm{cm}^{-3}$. This is expected, as these densities surpass the critical densities of all considered transitions, resulting in contour patterns similar to those seen in the protoplanetary disk model. In such regimes, the line ratios become insensitive to density variations and are primarily governed by temperature, preventing any meaningful diagnostic intercepts for density. This reinforces the conclusion that OCS line ratios are not suitable for probing high-density environments.

A similar limitation applies at the opposite end of the parameter space, specifically at low densities and high temperatures. In these conditions, collisional excitation is inefficient due to insufficient collision rates, and the molecular level populations are primarily influenced by the background radiation field. Consequently, the sensitivity of line ratios to temperature variations is significantly diminished, making reliable temperature diagnostics challenging. Therefore, no intercepts were expected–nor found–for line ratios in regions of low density and high temperature.

For the plateau component, the Galactic Center model was adopted, which captures the highly turbulent conditions with strong background radiation present in that part of Orion KL. The line-ratio intercepts for this component are presented in Fig. 7 (b). For this model, no trend was found that would highlight the importance of transitions with $J_\mathrm{u} < 10$ as for the plateau regions, but similar temperature and density ranges have been traced.

For the hot core, no intercepts were found with the protostellar envelope or model, indicating that the extreme physical conditions present in that region could not be well approximated.

3.3.3 DM Tau

In the case of the protoplanetary disk DM Tau, the line analysis was simplified by the fact that the disk's density modeled across the range given in Table 6 for the outer PPD region is significantly higher than the critical densities of the observed OCS transitions. As a result, the molecular line ratios are primarily sensitive to temperature with negligible dependence on density. This implies that, rather than requiring a temperature–density intersection for diagnostics, the kinetic temperature can be estimated using a single line ratio. More observed molecular lines would trace similar temperatures as the system is collisional due to the large densities, therefore, the recently observed OCS transitions of $J = 12 \rightarrow 11$ and $J = 18 \rightarrow 17$ in this protoplanetary disk by Semenov et al. [76] allow an approximate determination of the system's temperature. The peak values determined for the measured line intensities are given in Table 10.

Table 10: Peak intensities of OCS transitions observed by the ALMA observatory in DM Tau reported by Semenov et al. [76].

Transition	I_peak [mJy]
$12 \rightarrow 11$	≤ 130
$18 \rightarrow 17$	≤ 10

Applying the outer protoplanetary disk model, the derived kinetic temperature falls within the range $T_\mathrm{kin} \approx 10 - 20$ K for the maximum threshold intensities given in Table 10 (also see Fig. 11 in Appendix B), assuming a 50% uncertainty in the intensity values. This rough estimate is in good agreement with the previously derived temperature of $T_\mathrm{kin} = 13 - 20$ K for the outer layers based on CO observations [77].

3.4. Observing Proposal for L1157

To further support the potential of OCS as a reliable temperature and density tracer, an observation is proposed for the star-forming region L1157, which is known for its active molecular chemistry [78]. OCS lines have been detected and identified in this region, although their antenna temperatures have not been reported [79]. Due to its rich chemical activity, L1157 is a promising candidate for future temperature–density diagnostics and may support our hypothesis that OCS can serve as a reliable tracer of physical conditions in diverse astrophysical environments.

For this proposal, the IRAM 30m telescope was selected due to its capability to observe in two frequency bands simultaneously, significantly reducing the required observation time. The telescope is equipped with the EMIR (Eight Mixer Receiver) system, which supports simultaneous observations in the 3 mm, 2 mm, 1.3 mm, and 0.9 mm atmospheric windows–corresponding to the E090, E150, E230, and E330 bands, respectively [40]. The coordinates of the central protostar in L1157 are RA (J2000) = $20^{\mathrm{h}}39^{\mathrm{m}}06^{\mathrm{s}}$ and Dec (J2000) = $+68°02'16''$ [80], placing it within the circumpolar region for the telescope. This significantly simplifies scheduling for extended observations, as the source remains continuously visible and can be observed within a single time slot. The proposed observations are planned for the winter season to minimize atmospheric noise.

To use L1157 for further testing of OCS, first, the line transitions to be used for the diagnostics had to be selected based on several criteria. Since frequencies below 80 GHz are inaccessible to IRAM, the $J = 7 \rightarrow 6$ transition is the lowest that could be considered. To construct an efficient observing plan, Eq. 2.13 was used to estimate which OCS transitions could be observed with the shortest integration times, based on the line intensities modeled with `RADEX`. This estimation required knowledge of the radiation temperatures and a target signal-to-noise ratio.

For the radiation temperature modeling, `RADEX` was used with input parameters estimated from previous observations of L1157 based on the work of Burkhardt et al. [79]. The values adopted were $T_{\mathrm{kin}} = 60\,\mathrm{K}$, $N(\mathrm{OCS}) = 10^{14}\,\mathrm{cm}^{-2}$, $n_{\mathrm{H_2}} = 10^{5}\,\mathrm{cm}^{-3}$, $T_b = 2.73\,\mathrm{K}$, $\Delta V = 3\,\mathrm{km\ s}^{-1}$, and an optical depth model of β_{sphere}. As there are large temperature and density gradients in the outflows of L1157, these values serve only as rough estimates. The SNR was selected based on the prior diagnostic analysis for Sagittarius B2 and Orion KL, which demonstrated that accurate intercepts for distinct temperature and density combinations require relatively low uncertainties in the antenna temperatures. Hence, a SNR of 20 was adopted. Using the results of the `RADEX` modeled radiation temperatures, transitions with J_{u} between 7 and 17 produced the shortest integration times (approximately between 1 and 5 hours) based on Eq. 2.14, and were therefore selected for further analysis. Transitions beyond this range were excluded due to the significantly longer telescope time required.

Combining the E090 and E150 bands provides broad and efficient coverage of the desired transition range starting from the $J = 7 \rightarrow 6$ line. Since only two frequency bands can be observed simultaneously, transitions beyond $J = 13 \rightarrow 12$ were excluded to keep the total observation time realistic and to avoid the need for repeated observations with different band settings. Furthermore, the $J = 11 \rightarrow 10$ transition falls outside the observable frequency range due to atmospheric absorption. Consequently, the final set of selected transitions includes $J = 7 \rightarrow 6$, $J = 8 \rightarrow 7$, $J = 9 \rightarrow 8$, $J = 10 \rightarrow 9$, $J = 12 \rightarrow 11$, and $J = 13 \rightarrow 12$.

After finalizing the desired line transition range, the required telescope times for each line were estimated using the IRAM 30m time/sensitivity estimator[1]. The estimator requires specification of the observed frequency, the RMS noise σ_{T_A}, the spectral resolution, and the average elevation

[1]Link to the estimator: https://oms.iram.fr/tse/

of the target. The frequencies are determined by the selected transitions, and the values for σ_{T_A} were calculated from the predefined SNR and the modeled T_R values, incorporating the telescope's main beam efficiency. The spectral resolution was chosen to be the largest value that still allows the expected line widths to be resolved. Since the precise shape of the lines is not critical for this study and higher spectral resolution (i.e., smaller values) significantly increases telescope time, a resolution of 0.5 km s^{-1}, was selected, based on typical line widths (1-5 km s^{-1},) of other molecules observed in L1157 [79]. Since L1157 is circumpolar for the IRAM 30m telescope, its average elevation approximately equals the latitude of the observatory, which is +37°03′58″ N.

With the parameters defined, the estimator calculates both the off-source and on-source times required for the observation and estimates the total telescope time to be proposed, for which the choice of the tracking method is crucial. For this study, position switching was chosen, as it is more reliable than other tracking methods available for the telescope when lines are broadened by turbulence and outflows [40], which is expected in L1157. The total time estimates for each line transition are given in Table 11 based on the RMS uncertainty in the modeled radiation temperatures.

Table 11: Modeled radiation temperatures, estimated antenna temperature uncertainties, and the corresponding required telescope times for OCS line transitions with the shortest expected observation durations.

Transition	Freq. [GHz]	T_R [K]	σ_{T_A} [mK]	Time [h]
$7 \rightarrow 6$	85.1	0.236	8.25	**3.2**
$8 \rightarrow 7$	97.3	0.285	9.97	2.0
$9 \rightarrow 8$	109.5	0.330	11.54	2.0
$11 \rightarrow 10$	133.8	0.397	13.88	1.5
$12 \rightarrow 11$	145.9	0.415	14.52	1.4
$13 \rightarrow 12$	158.1	0.422	14.75	1.8

To study temperature and density variations across the shocked regions within the two jets, 5 different regions is proposed for observing L1157: 1-1 outer and 1-1 inner regions in the two jets, and 1 central observation to observe part of the protostellar envelope perpendicular to the jets. These regions were selected based on previous molecular studies of CO emission of the $J = 2 \rightarrow 1$ line transition from L1157 (see Fig. 8), which was also used to estimate the spatial extent of the regions where significant OCS emission could be observed. The four regions planned in the bipolar jet correspond to the B1 & B2 and the R0 & R1 outflows, where significant OCS molecular line emission is expected from the CO study by Bachiller et al. [78].

Overall, an estimated $5 \times 3.2 =$ **16 hours** of observing time is required for all lines to be detected within the 5 selected regions with the required SNR under average winter conditions, including the time required for tuning. The proposed observing regions are marked by green circles in Fig. 9. Each green circle has a diameter equal to the spatial resolution of the beam: 15.6" at the highest frequency of 158.1 GHz, corresponding to the highest resolution to ensure that all frequencies capture the entirety of the considered areas.

As the approximate temperatures and densities of the jets in L1157 are quite well known (see Burkhardt et al. [79]), this proposal would serve as a base for drawing more rigorous conclusions about the reliability of OCS as condition tracer rather than expecting an improvement for these values based on the OCS line emission observations.

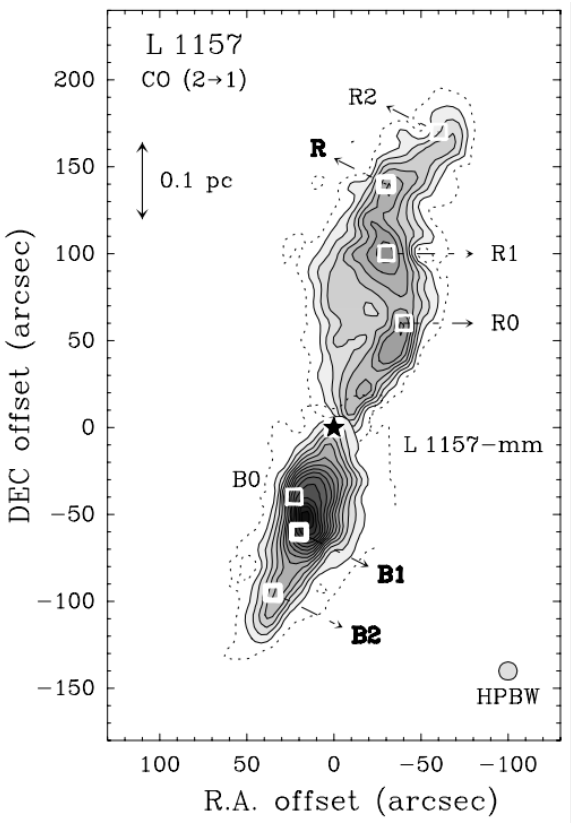

Figure 8: CO molecular line emission map of L1157; the black star denotes the position of the central protostar. The R and B labels indicate the red- (R) and blueshifted (B) lobes of the bipolar outflow, while the numbers (e.g., B0-B3, R0-R3) correspond to distinct shock events from episodic ejections. Image taken from the study of Bachiller et al. [78].

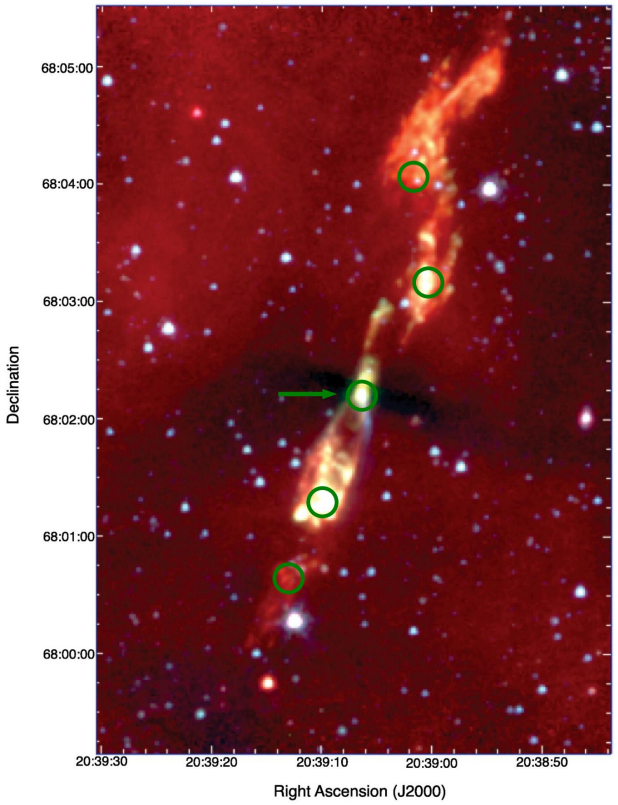

Figure 9: Infrared image of the L1157 outflow by the Spitzer Space Telescope's Infrared Array Camera (IRAC). The Spitzer image has infrared light of 8 microns colored red, 4.5-micron infrared light colored green, and 3.6-micron infrared light colored blue. The green circles mark the approximate position of the five selected regions for observation within the nebula, and the green arrow denotes the position of the central protostar. Image credit: NASA/JPL-Caltech/Harvard-Smithsonian CfA [81].

Chapter 4

Discussion

4.1. Non-LTE Line Modeling

The line analysis of OCS presented in this study offers valuable insights for tracing low-temperature and low-density regions, however, it is important to carefully consider several factors that may affect the interpretation of the results.

A key limitation in this study stems from the restricted availability of collisional rate coefficients at higher temperatures and for transitions involving large J values. The 1978 dataset provides rates up to 100 K for $J \leq 12$ (not including the extrapolation by Schöier et al. [33]), while the more recent 2023 dataset extends to 80 K for $J \leq 40$. Beyond these temperature ranges, `RADEX` does not perform extrapolation–instead, it defaults to using the downward rate coefficients at 80 K for higher temperatures in the case of the 2023 data. This introduces increased uncertainties in modeling warmer regions, such as protostellar envelopes and the inner regions of protoplanetary disks.

To quantify the impact of this limitation, the 2023 de-excitation rate coefficients were linearly extrapolated up to 500 K (the highest temperature considered in this study) using the rates at the two highest available temperature points, 60 K and 80 K (see Fig. 12 in Appendix C). Linear extrapolation appeared to provide a reasonable upper estimate of the impact, given that the temperature dependence of the rate coefficients decreases with increasing temperature. The extrapolated values were then compared with those at 80 K to assess the uncertainty associated with the use of constant coefficients above this threshold by `RADEX`. The resulting deviations for the rate coefficients remained within 30% for all transitions between $2 \rightarrow 1$ and $40 \rightarrow 39$, suggesting that the use of 80 K rates above this temperature still produces reasonably accurate results. Nevertheless, the need for reliable OCS collisional rate coefficients at higher temperatures remains evident.

The extrapolation method used by Schöier et al. [33] for the 1978 dataset is valid primarily in the regime where the kinetic energy of the colliding molecules greatly exceeds the energy spacing between rotational levels. As a result, the polynomial fitting approach applied in that work is expected to perform well for the H_2-OCS system, given the relatively small rotational energy splitting of OCS compared to other molecules commonly used in astrophysical diagnostics. However, this method still introduces uncertainties of up to 50% in many of the calculated rate coefficients [33]. The largest discrepancies reported in their study occurred in regions where extrapolation was applied in both temperature and energy levels. Consequently, uncertainties in the 1978 dataset are likely to be more significant than in the 2023 dataset, where extrapolation was only required for temperatures beyond the available data.

Additionally, this study focused solely on collisional excitation involving the H_2-OCS system, which simplifies the complex composition of astrophysical environments. In reality, other collisional partners–such as helium–can also play a non-negligible role in affecting line intensities. Including collisions with He would already improve the accuracy of line analysis, as H_2, although dominant, is not the only relevant species. As a first-order approximation, the contribution of helium can be accounted for by scaling the H_2 density by a factor of 1.14, assuming a typical He abundance of 20% relative to H_2 [33]. This scaling was not performed in this research, but should be accounted for in later studies.

Another important limitation was the use of fixed input parameters to model diverse astrophysical regions. Since these simplified models cannot fully describe the complexity and variability of real environments, their results should be viewed as general trends rather than precise templates. To improve the accuracy of diagnostics, observational constraints on column density and linewidth should be obtained for each specific region. These values could then be used as inputs to create more accurate `RADEX` models, enabling more robust constraints on the kinetic temperature and the H_2 number density.

In the case of the inner and outer protoplanetary disk models, the substantial radial and azimuthal variations were also neglected in this analysis. Protoplanetary disks are complex systems with strong gradients in temperature, density, and chemical composition both radially–from the hot, dense inner disk to the cooler outer regions–and azimuthally, due to structures like spiral arms and gaps. These spatial variations strongly influence molecular excitation and line emission. Proper interpretation of observations therefore requires more sophisticated modeling approaches that explicitly account for such spatial diversity. This could be achieved for example with `ProDiMo` (Protoplanetary Disk Model), which is a scientific software package used to model UV-photochemistry, ice formation, gas heating, disk structure, and radiative transfer in protoplanetary disks, developed by Woitke et al. [82]. Specifically for protoplanetary disks, `ProDiMo` would have the advantage compared to `RADEX` that it could be used to model a disk in 3D, which could allow for discovering the differences in molecular line emission in both radial and azimuthal directions.

4.2. Line Ratio Analysis

For the line ratio analysis across temperature–density grids, the selected useful lines were chosen based on approximate detectability, which depends on telescope-specific parameters such as system temperature and efficiencies. These parameters vary with observing frequency, but here were approximated using conservative estimates rather than frequency-dependent functions. As a result, the identified usable transition ranges may not be fully accurate. To avoid proposing observations of transitions that are undetectable within practical observational limits or underestimate the required integration times, future analyses should incorporate frequency-dependent instrumental characteristics from telescope manuals. This will ensure more reliable observational planning and more accurate determination of useful line transitions for temperature–density diagnostics.

The chosen temperature and density ranges also restrict the applicability of the analysis. Not all relevant astrophysical objects fall within the selected parameter space, even if they belong to the same category, such as star-forming regions. Although the five simplified models provide useful general trends, precise conclusions for specific regions require detailed, region-specific modeling.

The small energy spacing between adjacent rotational levels of OCS results in line ratios that change only subtly across the modeled temperature and density ranges. This characteristic requires precise measurements of line intensities for effective diagnostics. At the same time, it emphasizes the robustness of OCS as a tracer: significant variations in line ratios are likely to

indicate truly different physical conditions rather than measurement noise or modeling artifacts. Additionally, the close spacing of energy levels enhances temperature sensitivity, making OCS transitions particularly valuable for accurate temperature estimates.

Furthermore, because these lines lie close in frequency, it is generally possible to observe multiple rotational transitions within the same frequency band, more so than for many other molecules. This increases the number of observable lines and improves the reliability of temperature and density measurements. The presence of many closely spaced transitions is especially beneficial under non-LTE conditions, where level populations deviate from a single-temperature Boltzmann distribution. Different transitions respond in distinct ways to changes in temperature and density, so analyzing multiple lines together provides a more complete diagnostic of the underlying physical conditions.

4.3. Temperature–Density Diagnostics

For the temperature–density diagnostics, the same environmental models used in the line analysis were applied to observational data from Sagittarius B2, Orion KL, and DM Tau. However, these models do not reflect the full range of temperature and density variations within these regions. Since `RADEX` assumes uniform physical conditions throughout the source, intercepts indicating multiple parameter values must be interpreted cautiously, understanding that different rotational levels may be excited under different conditions within the same astrophysical object. In practice, many astrophysical regions show wide ranges of temperature and density due to turbulence, stellar feedback, and localized heating or cooling. For example, Sagittarius B2 is a molecular cloud in the Galactic Center subject to conditions significantly different from typical molecular clouds. Furthermore, it was not explored whether a Galactic Center or molecular cloud model better represents Sagittarius B2, and different model choices could produce different diagnostic outcomes.

The results from Orion KL suggest that OCS can be a feasible diagnostic tool in relatively low-temperature and low-density environments, specifically where $T_{\rm kin} \lesssim 200$ K and $n_{\rm H_2} \lesssim 10^6$ cm^{-3}. In the analysis, not all line ratios produced unique combinations of physical parameters–fewer than 80 useful intercepts were identified from over 3000 possible transition combinations. Some combinations yielded multiple intercepts, which were excluded from the results. The derived temperature–density intercepts span a broad range, reducing their diagnostic precision, though this is expected given that `RADEX` assumes a homogeneous medium with uniform temperature and density. Interestingly, lower-lying transitions appear more effective in probing the physical conditions in star-forming regions, though this trend may partly reflect the limited data availability rather than intrinsic properties. Nonetheless, these findings suggest that prioritizing such transitions in future observations could enhance the likelihood of obtaining interpretable diagnostic results.

It is also important to note that the regions for which OCS was useful as a diagnostic tool were not the only ones considered. Additional regions, such as W51 and the Orion KL hot core subregion, were examined using available antenna temperatures. For W51, the low number of reported antenna temperatures limited the ability to find temperature–density intercepts. In the Orion KL hot core, despite numerous antenna temperatures and many tested transition combinations, no intercepts were found. This likely results from the hot core having densities above the critical densities of the observed transitions, making these lines unsuitable tracers of the local physical conditions.

The relatively low critical densities of OCS transitions, ranging from approximately 10^2 cm^{-3} to 10^6 cm^{-3} for the frequencies considered in this study, mean that OCS primarily traces diffuse to

moderately dense regions. For instance, in the Orion KL models, line ratios became insensitive to density above 10^6 cm^{-3}, likely indicating saturation at these higher densities. While OCS remains useful for constraining conditions in many molecular clouds and star-forming regions, its usefulness may be greater as a complementary tracer rather than a standalone diagnostic.

Besides `ProDiMo`, another radiative transfer code, `LIME` (Line Modeling Engine) could be used to model not only protoplanetary disks, but any 3D astrophysical objects, including molecular clouds, outflows, and envelopes. `LIME` was developed by Brinch et al. [83], and has the advantage that it is not constrained by cylindrical or spherical symmetries; it can handle asymmetric input models. Using these codes could be better used for astrophysical diagnostics with OCS line transitions, as they can account for the 3D complexity of these objects.

Based on the observing proposal for L1157, achieving sufficiently high SNRs for even a limited number of OCS transitions will require significant telescope time. Based on the analysis of Sagittarius B2, well-defined temperature–density intercepts only appear for some regions when uncertainties in line intensities (antenna temperatures) are kept very low. Achieving these low uncertainties demands high SNRs, which in turn require long integration times and increased observation costs.

Chapter 5

Conclusion

This study employed `RADEX` to model the properties of OCS line transitions, providing valuable insights into the molecule's potential as a tracer of temperature and density across various astrophysical environments, including molecular clouds, protostellar envelopes, star-forming regions, and the Galactic Center. Modeling molecular line intensities enabled diagnostics of sources such as Sagittarius B2, Orion KL, and DM Tau, demonstrating the usability of OCS as a tracer of environmental conditions. The critical densities of the examined transitions constrain the applicability of OCS to environments with densities below $\sim 10^6$ cm^{-3}. Furthermore, since `RADEX` does not accurately approximate collisional data at significantly higher temperatures, OCS is expected to be a reliable tracer for regions with temperatures below ~ 100 K for the explored frequency range. Consequently, OCS is expected to be most useful for diagnostics in regions such as molecular clouds, star-forming regions, and the Galactic Center, where physical conditions remain within these approximate thresholds.

Temperature tracing at higher densities, such as those found in protoplanetary disks, remains a promising direction for future studies. However, tracing these environments using molecules under non-LTE conditions poses additional challenges because of the sensitivity of line transitions to background radiation. This often limits the accuracy of the determination of physical parameters, allowing only approximate estimates within certain ranges.

OCS appears to be a promising candidate for constraining physical conditions in various interstellar environments. Although this study is somewhat restricted by the explored parameter space and the limited availability of reported antenna temperatures for its line transitions, the adopted approach successfully demonstrated the molecule's potential as a diagnostic tool. Further testing through the proposed observations of L1157 could enable more rigorous conclusions about its effectiveness as a tracer of environmental conditions.

For future work, it is recommended that the astrophysical objects for which diagnostics are desired be explicitly modeled, rather than basing the diagnostics on simplified models. This could be done, for example, using 3D modeling with `ProDiMo` and `LIME`, which allow for more complex representations of protoplanetary disks and asymmetric molecular regions such as star-forming regions and outflows, including temperature and density gradients that are significantly harder to account for using `RADEX`. Solving the radiative transfer equations with such 3D modeling would lead to significantly more precise diagnostics using observed OCS line transitions.

Declaration on Generative AI Use

This study was conducted using various generative AI models, including ChatGPT, DeepSeek, and Mistral AI. These models assisted in developing the Python script `radex_grid.py` and optimizing code for data analysis. This included generating code to efficiently create the line analysis plots and diagnostic plots to identify unique temperature–density intercepts from line intensity ratio contours. Additionally, these AI models were employed to correct grammatical and structural errors in the text. However, it is important to note that these models were not used to generate the text of this thesis. They were also not involved in the development of the research ideas or in explicitly providing data or scientific information. For efficiently finding relevant research papers, the AI model Elicit was used.

References

[1] Gerhard Herzberg. "Historical remarks on the discovery of interstellar molecules". In: *Journal of the Royal Astronomical Society of Canada* 82 (1988), pp. 115–127. URL: https://api.semanticscholar.org/CorpusID:115374752.

[2] H. S. P. Müller, F. Schlöder, J. Stutzki, and G. Winnewisser. "The Cologne Database for Molecular Spectroscopy, CDMS: a useful tool for astronomers and spectroscopists". In: *Journal of Molecular Structure* 742.1-3 (2005), pp. 215–227. DOI: 10.1016/j.molstruc.2005.01.027.

[3] Peter Atkins, Julio de Paula, and James Keeler. *Atkins' Physical Chemistry*. 11th ed. Oxford, UK: Oxford University Press, 2018.

[4] L. Jr. Spitzer and William D. Cochran. "Rotational Excitation of Interstellar H_{2}". In: *The Astrophysical Journal* 186 (1973). URL: https://api.semanticscholar.org/CorpusID:119776225.

[5] B. Tercero, J. Cernicharo, J. R. Pardo, and J. R. Goicoechea. "A line confusion limited millimeter survey of Orion KL (I): Sulfur carbon chains". In: *Astronomy & Astrophysics* (2010).

[6] A. Potapov, H. Linz, J. Bouwman, W. Rocha, J. Martin, S. Wolf, Th. Henning, and H. Terada. "Simple molecules and complex chemistry in a protoplanetary disk: A JWST investigation of the highly inclined disk d216-0939". In: *Astronomy & Astrophysics* (2025).

[7] S. Martín, J. Martín-Pintado, R. Mauersberger, C. Henkel, and S. García-Burillo. "Sulfur Chemistry and Isotopic Ratios in the Starburst Galaxy NGC 253". In: *The Astrophysical Journal* 620.1 (2005), p. 210. URL: https://ui.adsabs.harvard.edu/abs/2005ApJ...620..210M/abstract.

[8] Jan M. Hollis and Bobby Lee Ulich. "Detection of new interstellar transitions of H, OCS, and H2CO and a search for interstellar fluorine". In: *The Astrophysical Journal* 214 (1977), p. 699. URL: https://api.semanticscholar.org/CorpusID:119830316.

[9] Jacob C. Laas and Paola Caselli. "Modeling sulfur depletion in interstellar clouds". In: *Astronomy & Astrophysics* 624 (2019), A108. DOI: 10.1051/0004-6361/201834446. eprint: https://doi.org/10.1051/0004-6361/201834446. URL: https://doi.org/10.1051/0004-6361/201834446.

[10] Arnaud Mahieux, Séverine Robert, Franklin P. Mills, Kandis Lea Jessup, Loïc Trompet, Shohei Aoki, A. Piccialli, J. Peralta, and Ann Carine Vandaele. "Update on SO2, detection of OCS, CS, CS2, and SO3, and upper limits of H2S and HOCl in the Venus mesosphere using SOIR on board Venus express". In: *Icarus* (2023). URL: https://api.semanticscholar.org/CorpusID:257891675.

[11] Emmanuel Lellouch. "Chemistry induced by the impacts: Observations". In: 1996. URL: https://api.semanticscholar.org/CorpusID:117726648.

[12] A. C. Adwin Boogert, Perry A. Gerakines, and Douglas C. B. Whittet. "Observations of the Icy Universe". In: *Annual Review of Astronomy and Astrophysics* 53 (2015), pp. 541–581. DOI: 10.1146/annurev-astro-082214-122348. URL: https://doi.org/10.1146/annurev-astro-082214-122348.

[13] Mohammad Saki, Erika L. Gibb, Boncho P. Bonev, Nathan X. Roth, Michael A. DiSanti, Neil Dello Russo, Ronald J. Vervack, Adam J. McKay, and Hideyo Kawakita. "Carbonyl Sulfide (OCS): Detections in Comets C/2002 T7 (LINEAR), C/2015 ER61 (PanSTARRS), and 21P/Giacobini–Zinner and Stringent Upper Limits in 46P/Wirtanen". In: *The Astronomical Journal* 160.4 (2020), p. 176. URL: https://iopscience.iop.org/article/10.3847/1538-3881/aba522.

[14] Young Chol Minh, Hauyu Baobab Liu, and Roberto Galván-Madrid. "CHEMICAL DIAGNOSTICS OF THE MASSIVE STAR CLUSTER-FORMING CLOUD G33.92+0.11. I. 13CS, CH3OH, CH3N, OCS, H2S, SO2, and SiO". In: *The Astrophysical Journal* 824 (2016). URL: https://api.semanticscholar.org/CorpusID:124534876.

[15] M. Hawkins, M. J. Almond, and A. J. Downs. In: *Journal of Physical Chemistry* 89 (1985), pp. 3326–3329.

[16] E. Isoniemi, M. Pettersson, L. Khriachtchev, J. Lundell, and M. Räsänen. "Infrared Spectroscopy of H2S and SH in Rare-Gas Matrixes". In: *The Journal of Physical Chemistry A* 103 (1999), p. 6967.

[17] Theodore P. Jr. Snow. "Ultraviolet Observations of Interstellar Molecules". In: *Proceedings of the International Astronomical Union* 1 (2005), pp. 175–186. URL: https://api.semanticscholar.org/CorpusID:121601727.

[18] Daniel I. Lucas, Casey J. Kavaliauskas, Mark A. Blitz, Dwayne E. Heard, and Julia H. Lehman. "Ab Initio and Statistical Rate Theory Exploration of the CH ($X^2\Pi$) + OCS Gas-Phase Reaction". In: *The Journal of Physical Chemistry A* 127.31 (2023). Published as part of the Journal of Physical Chemistry virtual special issue "Marsha I. Lester Festschrift", pp. 6509–6520. DOI: 10.1021/acs.jpca.3c01082. URL: https://doi.org/10.1021/acs.jpca.3c01082.

[19] Marco Padovani, Daniele Galli, Alexei V. Ivlev, Paola Caselli, and Andrea Ferrara. "Production of atomic hydrogen by cosmic rays in dark clouds". In: *Astronomy & Astrophysics* (2018).

[20] Paul. F. Goldsmith and Richard A. Linke. "A study of interstellar carbonyl sulfide". In: *The Astrophysical Journal* 245 (1980), pp. 482–494. URL: https://api.semanticscholar.org/CorpusID:121346023.

[21] Estelle Bayet, Jeremy Yates, and Serena Viti. "CS LINE PROFILES IN HOT CORES". In: *The Astrophysical Journal* 728 (2010). URL: https://api.semanticscholar.org/CorpusID:119184479.

[22] F. Daniel, J. Cernicharo, E. Roueff, M. Gerin, and M. L. Dubernet. "The Excitation of N_2H^+ in Interstellar Molecular Clouds. II. Observations". In: *The Astrophysical Journal* 667 (2007), pp. 980–1001. DOI: 10.1086/520915.

[23] M. Padovani, C. M. Walmsley, M. Tafalla, P. Hily-Blant, and G. Pineau des Forêts. "Hydrogen cyanide and isocyanide in prestellar cores". In: *Astronomy & Astrophysics* 534 (2011), A77. DOI: 10.1051/0004-6361/201117134.

[24] M. Gerin, J. R. Goicoechea, J. Pety, and P. Hily-Blant. "HCO mapping of the Horsehead: Tracing the illuminated dense molecular cloud surfaces". In: *Astronomy & Astrophysics* 494 (2009), pp. 977–985. DOI: 10.1051/0004-6361:200810933.

[25] A. Remijan, E. C. Sutton, L. E. Snyder, D. N. Friedel, S.-Y. Liu, and C.-C. Pei. "High-Resolution Observations of Methyl Cyanide (CH_3CN) Toward the Hot Core Regions W51e1/e2". In: *The Astrophysical Journal* 606 (2004), pp. 917–928. DOI: 10.1086/382031.

[26] S. Leurini, P. Schilke, K. M. Menten, D. R. Flower, J. T. Pottage, and L.-H. Xu. "Methanol as a diagnostic tool of interstellar clouds. I. Model calculations and application to molecular clouds". In: *Astronomy & Astrophysics* 422 (2004), pp. 573–585. DOI: 10.1051/0004-6361:20047046.

[27] S. Maret, C. Ceccarelli, E. Caux, A. G. G. M. Tielens, J. K. Jørgensen, E. van Dishoeck, A. Bacmann, A. Castets, B. Lefloch, L. Loinard, B. Parise, and F. L. Schöier. "The H_2CO abundance in the inner warm regions of low mass protostellar envelopes". In: *Astronomy & Astrophysics* 416 (2004), pp. 577–594. DOI: 10.1051/0004-6361:20034157.

[28] Douglas A. Prinslow and P. B. Armentrout. "Collision-induced dissociation of CS+2. Heat of formation of the CS radical". In: *The Journal of Chemical Physics* 94.5 (Mar. 1991), pp. 3563–3567. ISSN: 0021-9606. DOI: 10.1063/1.459779. eprint: https://pubs.aip.org/aip/jcp/article-pdf/94/5/3563/18991349/3563_1_online.pdf. URL: https://doi.org/10.1063/1.459779.

[29] M. Castillo et al. "OCS isomerization and dissociation kinetics from statistical models". In: *ResearchGate* (2024). URL: https://www.researchgate.net/publication/380362090_OCS_isomerization_and_dissociation_kinetics_from_statistical_models.

[30] Gaurav Sharma and Anirban Pathak. "Dissociation energies of astrophysically important MgO, SO, SiN and TiO molecules using multireference configuration interaction calculations". In: *Results in Physics* 22 (2021), p. 103998. DOI: 10.1016/j.rinp.2021.103998. URL: https://www.sciencedirect.com/science/article/abs/pii/S2211180421000604.

[31] Robin T. Garrod and Tyler Pauly. "ON THE FORMATION OF CO2 AND OTHER INTERSTELLAR ICES". In: *The Astrophysical Journal* 735 (2011). URL: https://api.semanticscholar.org/CorpusID:50795178.

[32] Sheldon Green and Sally Chapman. "Collisional Excitation of Interstellar Molecules: Linear Molecules CO, CS, OCS, and HC_3N". In: *The Astrophysical Journal Supplement Series* 37 (June 1978), pp. 169–194.

[33] F. L. Schöier, F. F. S. van der Tak, E. F. van Dishoeck, and J. H. Black. "An atomic and molecular database for analysis of submillimetre line observations". In: *Astronomy & Astrophysics* 432 (2005), pp. 369–379. DOI: 10.1051/0004-6361:20041729.

[34] Jorge Charry and Alexandre Tkatchenko. "van der Waals Radii of Free and Bonded Atoms from Hydrogen (Z = 1) to Oganesson (Z = 118)". In: *Journal of Chemical Theory and Computation* 20.17 (2024), pp. 7469–7478. DOI: 10.1021/acs.jctc.4c00784.

[35] Thomas Allmendinger. "The Elucidation of the Ground State in the H-Atom-Model of Niels Bohr and its Application on the Bond-Length Computation in the H-Molecule". In: *International Journal of Molecular and Theoretical Physics* 2.1 (2018). DOI: 10.35840/2631-4751/7521.

[36] Otoniel Denis-Alpizar, Cristian Guerra, and Ximena Zarate. "Rate coefficients for the rotational de-excitation of OCS by collision with He". In: *Astronomy & Astrophysics* 680 (2023), A113. DOI: 10.1051/0004-6361/202348272. URL: https://doi.org/10.1051/0004-6361/202348272.

[37] F. F. S. Van der Tak, J. H. Black, F. L. Schöier, D. J. Jansen, and E. F. van Dishoeck. "A computer program for fast non-LTE analysis of interstellar line spectra: With diagnostic plots to interpret observed line intensity ratios". In: *Astronomy & Astrophysics* 468.2 (2007), pp. 627–635. DOI: 10.1051/0004-6361:20066820.

[38] National Institute of Standards and Technology. *NIST Triatomic Spectral Database, Carbonyl Sulfide (OCS)*. https://physics.nist.gov/PhysRefData/MolSpec/Triatomic/Html/Tables/OCS.html. 2003.

[39] Thomas L. Wilson, Kristen Rohlfs, and Susanne Hüttemeister. *Tools of Radio Astronomy*. 5th ed. Berlin, Heidelberg: Springer-Verlag, 2009. ISBN: 978-3-540-85121-9. DOI: 10.1007/978-3-540-85122-6.

[40] J. Pety, S. Bardeau, and E. Reynier. *IRAM-30m EMIR time/sensitivity estimator*. Tech. rep. IRAM Memo 2009-1. Version 1.1. IRAM, 2010. URL: https://www.iram.fr/IRAMFR/GILDAS/doc/html/memo2009-1.pdf.

[41] A. G. G. M. Tielens. *The Physics and Chemistry of the Interstellar Medium*. Cambridge University Press, 2005. URL: https://search.ebscohost.com/login.aspx?direct=true&db=nlebk&AN=139595&site=ehost-live&scope=site.

[42] David Jona Jansen. "The Physical and Chemical Structure of Warm and Dense Molecular Clouds". PhD thesis. Leiden, The Netherlands: Rijksuniversiteit te Leiden, 1995.

[43] Donald E. Osterbrock and Gary J. Ferland. *Astrophysics of Gaseous Nebulae and Active Galactic Nuclei*. 2nd. Sausalito, CA: University Science Books, 2006.

[44] Dimitri Mihalas. *Stellar Atmospheres*. 2nd. San Francisco: W. H. Freeman and Company, 1978.

[45] T. De Jong, W. Boland, and A. Dalgarno. "Line formation in interstellar molecular clouds". In: *Astronomy and Astrophysics* 91 (1980), pp. 68–74.

[46] T. De Jong, A. Dalgarno, and W. Boland. "Escape probabilities and line formation in molecular clouds". In: *Astronomy and Astrophysics* 41 (1975), pp. 157–166.

[47] Nanase Harada, Yuri Nishimura, Yoshimasa Watanabe, Satoshi Yamamoto, Yuri Aikawa, Nami Sakai, and Takashi Shimonishi. "Molecular-cloud-scale Chemical Composition. III. Constraints of Average Physical Properties through Chemical Models". In: *The Astrophysical Journal* 871 (Feb. 2019), p. 238. DOI: 10.3847/1538-4357/aaf72a. URL: https://doi.org/10.3847/1538-4357/aaf72a.

[48] Paul F. Goldsmith and Richard A. Linke. "A Study of Interstellar Carbonyl Sulfide". In: *The Astrophysical Journal* 243 (1981), pp. L9–L12.

[49] A. Crapsi, Ewine F. van Dishoeck, M. R. Hogerheijde, K. M. Pontoppidan, and C. P. Dullemond. "Characterizing the nature of embedded young stellar objects through silicate, ice and millimeter observations". In: *Astronomy & Astrophysics* 486 (July 2008), pp. 245–254. DOI: 10.1051/0004-6361:20078589.

[50] Julia C. Santos, Martijn L. van Gelder, Pooneh Nazari, Aida Ahmadi, and Ewine F. van Dishoeck. "SO2 and OCS toward high-mass protostars: A comparative study between ice and gas". In: *Astronomy & Astrophysics* (July 2024). URL: https://arxiv.org/pdf/2407.14711.

[51] W. H. McCutcheon, T. Sato, C. R. Purton, H. E. Matthews, and P. E. Dewdney. "Millimeter and Submillimeter Wavelength Continuum Observations of Massive Young Stellar Objects". In: *The Astronomical Journal* 110.4 (Oct. 1995). DOI: https://articles.adsabs.harvard.edu/pdf/1995AJ....110.1762M.

[52] Adam Ginsburg, Christian Henkel, Yiping Ao, Denise Riquelme, Jens Kauffmann, Thushara Pillai, Elisabeth A. C. Mills, Miguel A. Requena-Torres, Katharina Immer, Leonardo Testi, Juergen Ott, John Bally, Cara Battersby, Jeremy Darling, Susanne Aalto, Thomas Stanke, Sarah Kendrew, J. M. Diederik Kruijssen, Steven Longmore, James Dale, Rolf Guesten, and Karl M. Menten. "Dense gas in the Galactic central molecular zone is warm and heated by turbulence". In: *Astronomy & Astrophysics* 586 (2016), A50. DOI: 10.1051/0004-6361/201526100.

[53] P. M. Solomon, A. A. Penzias, K. B. Jefferts, and R. W. Wilson. "Millimeter Emission Lines of Polyatomic Molecules in Sagittarius B2". In: *The Astrophysical Journal* 185 (Oct. 1973), pp. L63–L66. DOI: 10.1086/181325.

[54] H. Nomura and T. J. Millar. "Molecular hydrogen emission from protoplanetary disks". In: *Astronomy & Astrophysics* 438 (2005), pp. 923–938. DOI: 10.1051/0004-6361:20052809. URL: https://doi.org/10.1051/0004-6361:20052809.

[55] Anne Dutrey, Dmitry Semenov, Edwige Chapillon, Uma Gorti, Stéphane Guilloteau, Franck Hersant, Michiel Hogerheijde, Meredith Hughes, Gwendolyn Meeus, Hideko Nomura, Vincent Piétu, Chunhua Qi, and Valentine Wakelam. "Physical and chemical structure of planet-forming disks probed by millimeter observations and modeling". In: *Protostars and Planets VI*. Ed. by H. Beuther, R. S. Klessen, C. P. Dullemond, and Th. Henning. University of Arizona Press, 2014, pp. 317–338. DOI: 10.2458/azu_uapress_9780816531240-ch014. URL: https://doi.org/10.48550/arXiv.1402.3503.

[56] M. L. Kutner, P. Thaddeus, A. A. Penzias, R. W. Wilson, and K. B. Jefferts. "New interstellar methanol lines". In: *The Astrophysical Journal Letters* 183 (July 1973), pp. L27–L30. DOI: 10.1086/181195.

[57] A. C. A. Boogert, K. Brewer, A. Brittain, and K. S. Emerson. "Survey of ices toward massive young stellar objects. I. OCS, CO, OCN^-, and CH_3OH". In: *The Astrophysical Journal* 941.1 (Dec. 2022), p. 32. DOI: 10.3847/1538-4357/ac9b4a. URL: https://doi.org/10.3847/1538-4357/ac9b4a.

[58] GBT Science Support Staff. *The Performance of the GBT: A Guide for Planning Observations*. Revised: Nov. 1, 2009; Cosmetic revisions: Nov. 28, 2017; Jan. 26, 2021; June 15, 2021. 2005. URL: https://www.gb.nrao.edu/GBT/Performance/PlaningObservations.htm.

[59] Jeff Mangum. *ALMA Sensitivity Metric for Science Sustainability Projects*. Tech. rep. ALMA Memo 602, Doc#: ALMA-35.00.101.666-A-SPE. Status: Finito. Version 6, dated 2017-01-23. ALMA Project Office, Jan. 2017. URL: https://library.nrao.edu/public/memos/alma/main/memo602.pdf.

[60] A. M. Baryshev, R. Hesper, F. P. Mena, T. M. Klapwijk, T. A. van Kempen, M. R. Hogerheijde, B. D. Jackson, J. Adema, G. J. Gerlofsma, M. E. Bekema, and et al. "The ALMA Band 9 receiver: Design, construction, characterization, and first light". In: *Astronomy & Astrophysics* 577 (2015), A129. DOI: 10.1051/0004-6361/201425529.

[61] J. Pety, J. Boissier, E. Reynier, and S. Bardeau. *NOEMA Sensitivity Estimator*. Tech. rep. IRAM Memo 2015-3. Version 3.1, July 22nd. IRAM (Grenoble), 2019.

[62] M. Krips. *An Introduction to the IRAM NOEMA Interferometer*. Version 6.0–00 (Aug. 2, 2019). Institut de Radioastronomie Millimétrique (IRAM). 2019. URL: https://www.iram.fr/IRAMFR/GILDAS/doc/html/noema-intro-html/noema-intro.html.

[63] National Radio Astronomy Observatory (NRAO). *ngVLA Performance Estimates*. https://ngvla.nrao.edu/page/performance. Next Generation Very Large Array (ngVLA), Dec. 2021.

[64] Enrique Vázquez-Semadeni, Dongsu Ryu, Thierry Passot, Ricardo F. González, and Adriana Gazol. "Molecular Cloud Evolution. I. Molecular Cloud and Thin Cold Neutral Medium Sheet Formation". In: *The Astrophysical Journal* 643 (May 2006), pp. 245–259. DOI: 10.1086/501499. URL: https://doi.org/10.1086/501499.

[65] Robert B. Loren, Aa. Sandqvist, and A. Wootten. "Molecular Clouds on the Threshold of Star Formation: The Radial Density Profile of the Cores of the Rho Ophiuchi and R Coronae Australis Clouds". In: *The Astrophysical Journal* 270 (July 1983), pp. 620–640. DOI: 10.1086/161154. URL: https://doi.org/10.1086/161154.

[66] M. Rowan-Robinson. "Clouds of Dust and Molecules in the Galaxy". In: *The Astrophysical Journal* 234 (Nov. 1979), pp. 111–128. DOI: 10.1086/157487. URL: https://doi.org/10.1086/157487.

[67] Shigehisa Takakuwa, Takeshi Kamazaki, Masao Saito, Nobuyuki Yamaguchi, and Kotaro Kohno. "ASTE Observations of Warm Gas in Low-mass Protostellar Envelopes: Different Kinematics between Submillimeter and Millimeter Lines". In: *Publications of the Astronomical Society of Japan* (2006). Received 2006 May 22; accepted 2006 July 29. URL: https://pasj.jp/journals/.

[68] Adam Ginsburg, Christian Henkel, Yiping Ao, Denise Riquelme, Jens Kauffmann, Thushara Pillai, Elisabeth A. C. Mills, Miguel A. Requena-Torres, Katharina Immer, Leonardo Testi, Juergen Ott, John Bally, Cara Battersby, Jeremy Darling, Susanne Aalto, Thomas Stanke, Sarah Kendrew, J. M. Diederik Kruijssen, Steven Longmore, James Dale, Rolf Guesten, and Karl M. Menten. "Dense Gas in the Galactic Central Molecular Zone is Warm and Heated by Turbulence?" In: *Astronomy & Astrophysics* 586 (2016), A50. DOI: 10.1051/0004-6361/201526100. URL: https://doi.org/10.1051/0004-6361/201526100.

[69] H. Nomura and T. J. Millar. "Molecular hydrogen emission from protoplanetary disks". In: *Astronomy & Astrophysics* 438 (2005), pp. 923–938. DOI: 10.1051/0004-6361:20052809. URL: https://doi.org/10.1051/0004-6361:20052809.

[70] Jürgen Ott, Axel Weiß, Lister Staveley-Smith, Christian Henkel, and David S. Meier. "ATCA Survey of Ammonia in the Galactic Center: The Temperatures of Dense Gas Clumps Between Sgr A* and Sgr B2". In: *The Astrophysical Journal* 786.2 (2014). DOI: 10.1088/0004-637X/786/2/91. arXiv: 1402.4531 [astro-ph.GA]. URL: https://doi.org/10.48550/arXiv.1402.4531.

[71] Richard A. Linke, S. E. Cummins, Sheldon Green, and Patrick Thaddeus. "Methyl Cyanide as a Probe of the Temperature and Density in SgrB2; Quasi-Equilibrium in Molecular Rotational Levels". In: 1982. URL: https://api.semanticscholar.org/CorpusID:93604642.

[72] Y. Gong, C. Henkel, S. Thorwirth, S. Spezzano, K. M. Menten, C. M. Walmsley, F. Wyrowski, R. Q. Mao, and B. Klein. "A 1.3 cm line survey toward Orion KL". In: *Astronomy & Astrophysics* 581 (2015), A48. DOI: 10.1051/0004-6361/201526275. URL: https://doi.org/10.1051/0004-6361/201526275.

[73] B. Tercero, J. Cernicharo, J. R. Pardo, and J. R. Goicoechea. "A line confusion limited millimeter survey of Orion KL (I): sulfur carbon chains". In: *Astronomy & Astrophysics* 517 (2010), A96. DOI: 10.1051/0004-6361/201014149. URL: https://doi.org/10.1051/0004-6361/201014149.

[74] D. N. Friedel and S. L. Widicus Weaver. "Complex Organic Molecules at High Spatial Resolution toward Orion-KL. II. Kinematics". In: *The Astrophysical Journal Supplement Series* 201.2 (2012), p. 17. DOI: 10.1088/0067-0049/201/2/17. URL: https://doi.org/10.1088/0067-0049/201/2/17.

[75] Dan M. Watson, Reinhard Genzel, Charles H. Townes, and J. M. V. Storey. *Far-Infrared Emission Lines of CO and OH in the Orion-KL Molecular Shock*. NASA Technical Memorandum 86721. NASA Ames Research Center, 1985.

[76] D. Semenov, C. Favre, D. Fedele, S. Guilloteau, R. Teague, Th. Henning, A. Dutrey, E. Chapillon, F. Hersant, and V. Piétu. "Chemistry in disks XI. Sulfur-bearing species as tracers of protoplanetary disk physics and chemistry: the DM Tau case". In: *Astronomy & Astrophysics* 617 (2018), A28. DOI: 10.1051/0004-6361/201832980. URL: https://doi.org/10.1051/0004-6361/201832980.

[77] E. Dartois, A. Dutrey, and S. Guilloteau. "Structure of the DM Tau Outer Disk: Probing the vertical kinetic temperature gradient". In: *Astronomy & Astrophysics* 399 (2003), pp. 773–787. DOI: 10.1051/0004-6361:20021638. URL: https://doi.org/10.1051/0004-6361:20021638.

[78] R. Bachiller, M. Pérez Gutiérrez, M. S. N. Kumar, and M. Tafalla. "Chemically active outflow L 1157". In: *Astronomy & Astrophysics* 372 (2001), pp. 899–912. DOI: 10.1051/0004-6361:20010519.

[79] Andrew M. Burkhardt, Niklaus M. Dollhopf, Joanna F. Corby, P. Brandon Carroll, Christopher N. Shingledecker, Ryan A. Loomis, Shawn Thomas Booth, Geoffrey A. Blake, Eric Herbst, Anthony J. Remijan, and Brett A. McGuire. "CSO and CARMA Observations of L1157. II. Chemical Complexity in the Shocked Outflow". In: *The Astrophysical Journal* 827.1 (Aug. 2016), p. 21. DOI: 10.3847/0004-637X/827/1/21. URL: https://doi.org/10.3847/0004-637X/827/1/21.

[80] John J. Tobin, Erin G. Cox, and Leslie W. Looney. "A 16 au Binary in the Class 0 Protostar L1157 MMS". In: *The Astrophysical Journal* 928.1 (2022), p. 61. DOI: 10.3847/1538-4357/ac5594. URL: https://doi.org/10.3847/1538-4357/ac5594.

[81] NASA, JPL-Caltech, and Leslie Looney. *Spitzer spies young star*. https://astronomy.com/news/2007/11/spitzer-spies-young-star. 2007.

[82] Peter Woitke, Inga Kamp, and Wing-Fai Thi. "Radiation thermo-chemical models of protoplanetary disks. I. Hydrostatic disk structure and inner rim". In: *Astronomy & Astrophysics* 501.1 (2009), pp. 383–406. DOI: 10.1051/0004-6361/200911821.

[83] C. Brinch and M. R. Hogerheijde. "LIME – a flexible, non-LTE line excitation and radiation transfer method for millimeter and far-infrared wavelengths". In: *Astronomy & Astrophysics* 523 (2010), A25. DOI: 10.1051/0004-6361/201015333.

Appendix A: Critical Densities

Table 12: Calculated critical densities for various OCS rotational line transitions at selected temperatures using the 1978 dataset.

Transition	Upper	Lower	10 K	100 K	500 K
1	2	1	9.2e+01	1.1e+02	1.1e+02
2	3	2	6.2e+02	5.5e+02	5.4e+02
3	4	3	1.8e+03	1.7e+03	1.7e+03
4	5	4	4.9e+03	4.4e+03	4.2e+03
5	6	5	8.3e+03	8.2e+03	8.1e+03
6	7	6	1.5e+04	1.4e+04	1.4e+04
7	8	7	2.3e+04	2.1e+04	2.0e+04
8	9	8	3.8e+04	3.1e+04	3.1e+04
9	10	9	5.4e+04	4.5e+04	4.4e+04
10	11	10	7.5e+04	6.2e+04	6.0e+04
11	12	11	9.9e+04	8.1e+04	7.7e+04
12	13	12	1.3e+05	1.0e+05	9.8e+04
13	14	13	1.6e+05	1.5e+05	1.4e+05
14	15	14	1.9e+05	1.9e+05	1.7e+05
15	16	15	2.4e+05	2.3e+05	2.1e+05
16	17	16	3.0e+05	2.8e+05	2.6e+05
17	18	17	3.5e+05	3.4e+05	3.1e+05
18	19	18	4.2e+05	4.0e+05	3.7e+05
19	20	19	5.0e+05	4.8e+05	4.4e+05
20	21	20	5.9e+05	5.6e+05	5.1e+05
21	22	21	6.8e+05	6.5e+05	5.9e+05
22	23	22	8.0e+05	7.5e+05	6.8e+05
23	24	23	9.1e+05	8.5e+05	7.8e+05
24	25	24	1.1e+06	9.7e+05	8.8e+05
25	26	25	1.2e+06	1.1e+06	1.0e+06
26	27	26	1.4e+06	1.2e+06	1.1e+06
27	28	27	1.5e+06	1.4e+06	1.2e+06
28	29	28	1.7e+06	1.5e+06	1.4e+06
29	30	29	1.9e+06	1.7e+06	1.5e+06
30	31	30	2.2e+06	1.9e+06	1.7e+06
31	32	31	2.4e+06	2.1e+06	1.9e+06
32	33	32	2.7e+06	2.3e+06	2.1e+06
33	34	33	2.9e+06	2.5e+06	2.3e+06
34	35	34	3.2e+06	2.8e+06	2.5e+06
35	36	35	3.5e+06	3.0e+06	2.7e+06
36	37	36	3.9e+06	3.4e+06	3.0e+06
37	38	37	4.2e+06	3.7e+06	3.2e+06
38	39	38	4.7e+06	4.0e+06	3.5e+06
39	40	39	5.1e+06	4.3e+06	3.8e+06

Table 13: Calculated critical densities for various OCS rotational line transitions at selected temperatures using the 2023 dataset.

Transition	Upper	Lower	10 K	40 K	80 K
1	2	1	1.6e+02	2.1e+02	2.1e+02
2	3	2	5.8e+02	8.1e+02	8.5e+02
3	4	3	1.7e+03	2.1e+03	2.2e+03
4	5	4	4.0e+03	4.6e+03	4.8e+03
5	6	5	8.2e+03	9.3e+03	9.5e+03
6	7	6	1.5e+04	1.7e+04	1.7e+04
7	8	7	2.3e+04	2.7e+04	2.8e+04
8	9	8	3.5e+04	4.0e+04	4.2e+04
9	10	9	5.0e+04	5.8e+04	6.0e+04
10	11	10	6.8e+04	7.9e+04	8.2e+04
11	12	11	9.0e+04	1.1e+05	1.1e+05
12	13	12	1.2e+05	1.4e+05	1.4e+05
13	14	13	1.5e+05	1.7e+05	1.8e+05
14	15	14	1.8e+05	2.1e+05	2.3e+05
15	16	15	2.3e+05	2.6e+05	2.8e+05
16	17	16	2.8e+05	3.2e+05	3.4e+05
17	18	17	3.3e+05	3.8e+05	4.0e+05
18	19	18	4.0e+05	4.5e+05	4.8e+05
19	20	19	4.7e+05	5.4e+05	5.6e+05
20	21	20	5.5e+05	6.4e+05	7.0e+05
21	22	21	6.5e+05	7.2e+05	7.6e+05
22	23	22	7.5e+05	8.3e+05	8.8e+05
23	24	23	8.6e+05	9.5e+05	1.0e+06
24	25	24	9.9e+05	1.1e+06	1.1e+06
25	26	25	1.1e+06	1.2e+06	1.3e+06
26	27	26	1.3e+06	1.4e+06	1.5e+06
27	28	27	1.4e+06	1.6e+06	1.6e+06
28	29	28	1.6e+06	1.7e+06	1.8e+06
29	30	29	1.8e+06	1.9e+06	2.0e+06
30	31	30	2.1e+06	2.2e+06	2.2e+06
31	32	31	2.3e+06	2.4e+06	2.5e+06
32	33	32	2.6e+06	2.6e+06	2.7e+06
33	34	33	2.8e+06	2.9e+06	3.0e+06
34	35	34	3.1e+06	3.2e+06	3.3e+06
35	36	35	3.5e+06	3.5e+06	3.6e+06
36	37	36	3.8e+06	3.8e+06	3.9e+06
37	38	37	4.2e+06	4.2e+06	4.3e+06
38	39	38	4.6e+06	4.5e+06	4.7e+06
39	40	39	5.0e+06	4.9e+06	5.0e+06

Appendix B: Diagnostic Plots for Sagittarius B2 & DM Tau

Diagnostic Plots for Sagittarius B2

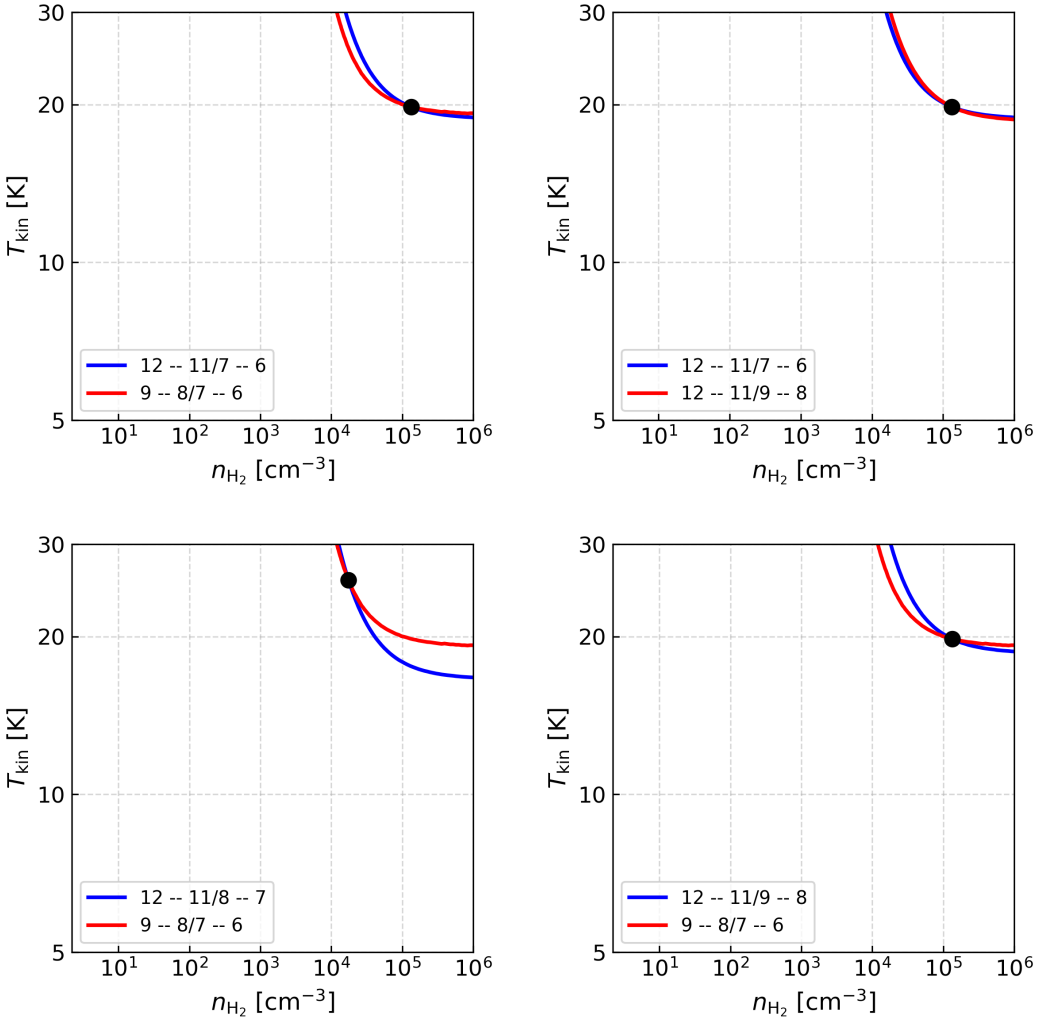

Figure 10: Diagnostic plots for Sagittarius B2 using the molecular cloud model. The contour lines represent the ratio of antenna temperature values reported by Solomon et al. [53].

Diagnostic Plot for DM Tau

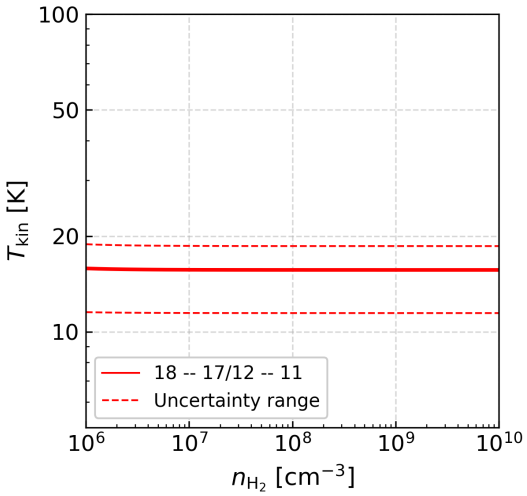

Figure 11: Diagnostic plot for DM Tau using the outer PPD model. The contour lines represent the ratio of the two antenna temperatures reported by Semenov et al. [76].

Appendix C: Extrapolated Rate Coefficients

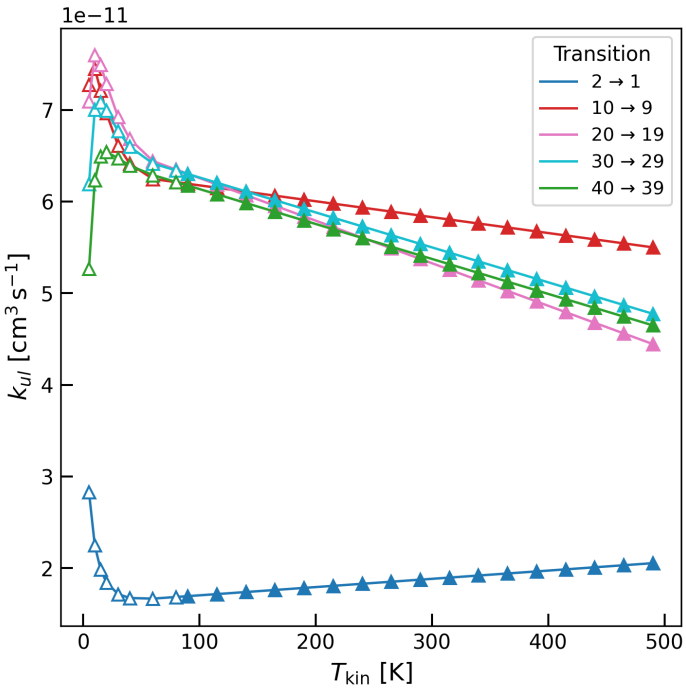

Figure 12: De-excitation rate coefficients from the 2023 dataset for some OCS transitions from Denis-Alpizar et al. [36] shown as empty triangles, with linear extrapolations up to 500 K based on the coefficients at 60 K and 80 K indicated by filled triangles.

Appendix D: Source Code for `radex_grid.py`

```python
import numpy as np
import os
import subprocess

def read_input_file():
    base_path = "/Users/DELL/AstroThesis/radex/data/"
    file_name = input("Enter the molecular data filename (e.g., OCS.txt): ")
    return os.path.join(base_path, file_name)

def get_user_inputs():
    print("Please provide the following inputs:")
    num_partners = int(input("Number of collisional partners: "))
    partner_name = input("Name of collisional partner (e.g., H2): ")
    background_temp = float(input("Background temperature (K): "))
    column_density = float(input("Molecular column density (cm^-2): "))
    line_width = float(input("Line width (km/s): "))

    # Frequency range inputs
    freq_low = float(input("Lower bound for frequency (GHz): "))
    freq_high = float(input("Upper bound for frequency (GHz): "))

    # Temperature grid inputs
    T_low = float(input("Lower bound for temperature (K): "))
    T_high = float(input("Upper bound for temperature (K): "))

    # Number density grid inputs
    n_low = float(input("Lower bound for number density (cm^-3): "))
    n_high = float(input("Upper bound for number density (cm^-3): "))

    # Number of grid points (same for both temperature and density)
    grid_points = int(input("Number of grid points (used for both T and n): "))

    return num_partners, partner_name, background_temp, column_density, line_width, freq_low, freq_high, T_low, T_high, n_low, n_high, grid_points

def generate_grid(T_low, T_high, n_low, n_high, grid_points):
    """
    Generate a grid of temperature and number density values.
    """
    temperatures = np.linspace(T_low, T_high, num=grid_points)  # Temperature grid
    densities = np.logspace(np.log10(n_low), np.log10(n_high), num=grid_points)  # Density grid (log scale)
    return [(T, n) for T in temperatures for n in densities]

def compute_line_intensities():
    print("Starting computation...")
    input_file = read_input_file()
    results_dir = "/Users/DELL/AstroThesis/radex/results"  # Results folder
    # Get user inputs
    num_partners, partner_name, background_temp, column_density, line_width, freq_low, freq_high, T_low, T_high, n_low, n_high, grid_points = get_user_inputs()

    # Generate the grid
    grid = generate_grid(T_low, T_high, n_low, n_high, grid_points)

    # Ensure the results directory exists
    os.makedirs(results_dir, exist_ok=True)

    flow = freq_low
    fupp = freq_high

    for T, n in grid:
        output_file = f"results_T{T:.1f}_n{n:.1e}.txt"
        output_file_path = os.path.join(results_dir, output_file)

        radex_input = f"""
{input_file}            # Molecular data file
{output_file_path}      # Output file name
{flow} {fupp}           # Min and max output frequencies in GHz
{T}                     # Kinetic temperature
{num_partners}          # Number of collision partners
{partner_name}          # Type of collision partner
{n}                     # Density of collision partner
{background_temp}       # Background temperature
{column_density}        # Molecular column density
{line_width}            # Line width
0                       # Another calculation [0/1]
"""
        input_path = "C:/Users/DELL/AstroThesis/radex/bin/radex_input.txt"
        with open(input_path, "w") as f:
            f.write(radex_input)

        radex_exe = r"C:/Users/DELL/AstroThesis/radex/bin/radex.exe"

        with subprocess.Popen([radex_exe], stdin=subprocess.PIPE, stdout=subprocess.PIPE, stderr=subprocess.PIPE) as proc:
            proc.communicate(input="\n".join([
                input_file,
                output_file_path,
                f"{flow:.3E} {fupp:.3E}",
                str(T),
                str(num_partners),
                partner_name,
                str(n),
                str(background_temp),
                str(column_density),
                str(line_width),
                "0"
            ]).encode())

    print("Computation finished. Results saved in:", results_dir)

if __name__ == "__main__":
    compute_line_intensities()
```